AFRL-SR-BL-TR-98-

0369

REDUCED-ENCODING DYNAMIC IMAGING

BY

JILL MARIE HANSON

B.E.E., University of Dayton, 1989
M.S., Stanford University, 1991

THESIS

Submitted in partial fulfillment of the requirements
for the degree of Doctor of Philosophy in Electrical Engineering
in the Graduate College of the
University of Illinois at Urbana-Champaign, 1997

Urbana, Illinois

19980430 162

REPORT DOCUMENTATION PAGE

AFRL-SR-BL-TR-98-

0369

Public reporting burden for this collection of information is estimated to average 1 hour per response, including tl
and maintaining the data needed, and completing and reviewing the collection of information. Send commen
information, including suggestions for reducing this burden, to Washington Headquarters Services, Directorate fc
1204, Arlington, VA 22202-4302, and to the Office of management and Budget, Paperwork Reduction Project (07C

:hering
tion of
, Suite

1. AGENCY USE ONLY (Leave Blank)	2. REPORT DATE April 1997	3. REPOF Final

4. TITLE AND SUBTITLE Reduced-Encoding Dynamic Imaging	5. FUNDING NUMBERS
6. AUTHORS Jill Marie Hanson	
7. PERFORMING ORGANIZATION NAME(S) AND ADDRESS(ES) University of Illinois at Urbana-Champaign	8. PERFORMING ORGANIZATION REPORT NUMBER
9. SPONSORING/MONITORING AGENCY NAME(S) AND ADDRESS(ES) AFOSR/NI 110 Duncan Avenue, Room B-115 Bolling Air Force Base, DC 20332-8080	10. SPONSORING/MONITORING AGENCY REPORT NUMBER
11. SUPPLEMENTARY NOTES	
12a. DISTRIBUTION AVAILABILITY STATEMENT Approved for Public Release	12b. DISTRIBUTION CODE
13. ABSTRACT *(Maximum 200 words)* See attached.	
14. SUBJECT TERMS	15. NUMBER OF PAGES
	16. PRICE CODE

17. SECURITY CLASSIFICATION OF REPORT Unclassified	18. SECURITY CLASSIFICATION OF THIS PAGE Unclassified	19. SECURITY CLASSIFICATION OF ABSTRACT Unclassified	20. LIMITATION OF ABSTRACT UL

DTIC QUALITY INSPECTED 4

Standard Form 298 (Rev. 2-89)
Prescribed by ANSI Std. 239.18
Designed using WordPerfect 6.1, AFOSR/XPP, Oct 96

REDUCED-ENCODING DYNAMIC IMAGING

BY

JILL MARIE HANSON

B.E.E., University of Dayton, 1989
M.S., Stanford University, 1991

THESIS

Submitted in partial fulfillment of the requirements
for the degree of Doctor of Philosophy in Electrical Engineering
in the Graduate College of the
University of Illinois at Urbana-Champaign, 1997

Urbana, Illinois

UNIVERSITY OF ILLINOIS AT URBANA-CHAMPAIGN

THE GRADUATE COLLEGE

APRIL 1997
(date)

WE HEREBY RECOMMEND THAT THE THESIS BY

JILL MARIE HANSON

ENTITLED REDUCED-ENCODING DYNAMIC IMAGING

BE ACCEPTED IN PARTIAL FULFILLMENT OF THE REQUIREMENTS FOR

THE DEGREE OF DOCTOR OF PHILOSOPHY

Director of Thesis Research

N. Narayana Rao
Head of Department

Committee on Final Examination†

Chairperson

Paul C Lauterbur

R. L. Magin

T S Huang

† Required for doctor's degree but not for master's.

O-517

ABSTRACT

This research addresses the problem of acquiring a time series of magnetic resonance images with both high spatial and temporal resolutions. Specifically, we systematically investigate the advantages and limitations of reduced-encoding imaging using *a priori* constraints. This study reveals that if the available *a priori* information is a reference image, direct use of this information to "optimize" data acquisition using the existing wavelet transform or singular value decomposition schemes can undermine the capability to detect new image features. However, proper incorporation of the *a priori* information in the image reconstruction step can significantly reduce the resolution loss associated with reduced-encoding. For Fourier-encoded data, we have shown that the generalized-series (GS) model is an effective mathematical framework for carrying out the constrained reconstruction step.

Several techniques are proposed in this dissertation to improve the basis functions of the GS model by introducing dynamic information. The two-reference reduced-encoding imaging by generalized-series reconstruction (TRIGR) method suppresses background information through the use of a second high-resolution reference image. A second technique injects information from the dynamic data into the GS basis functions, as opposed to deriving them solely from the reference information. These techniques allow the GS basis functions to more accurately represent the areas of dynamic change. Finally, motion that occurs between the acquisition of the reference and dynamic data sets can render the reference information useless as a constraint for image reconstruction. A motion compensation method is proposed which uses a similarity norm to accurately detect the motion in spite of contrast changes and the low-resolution nature of the dynamic data.

ACKNOWLEDGMENTS

I could not have successfully completed this work without the help and support of a great number of people. I would like to mention a few here, although the list is by no means complete.

I would like to thank the Air Force Laboratory Graduate Fellowship program and the Army Breast Cancer Research Predoctoral Fellowship program for supporting me financially through much of my graduate education.

I am deeply indebted to my advisors, Professors Zhi-Pei Liang and Paul Lauterbur, for their support and guidance throughout the course of this research. I would also like to express my gratitude to Professors Tom Huang and Richard Magin for serving on my doctoral committee.

I would like to thank my many friends and colleagues at BMRL, BRL and MREL, especially Chris Hess, for helpful discussions.

My deepest appreciation goes to my family and my husband's family for their understanding and assistance through the many years of college. In particular, I would like to thank my mom, the tireless grandma babysitter, without whose help I could have never finished this degree.

And most of all, I would like to thank my husband, Reed, for his love and support.

TABLE OF CONTENTS

LIST OF FIGURES

LIST OF SYMBOLS AND ABBREVIATIONS

$\in$	In a set
$\notin$	Not in a set
$\parallel A \parallel_2$	L_2 norm of matrix A with entries a_{ij} $\quad \parallel A \parallel_2 \doteq \sqrt{\sum_{i=0}^{m-1} \sum_{j=0}^{n-1} \lvert a_{ij} \rvert^2}$
$\mathcal{F}\{\cdot\}$	Fourier transform of $\cdot$
DRT	Data replacement technique
FFT	Fast Fourier Transform
FOV	Field of view
GS	Generalized series
MR	Magnetic resonance
MRI	Magnetic resonance imaging
PSF	Point spread function
RF	Radio frequency
RIGR	Reduced-encoding Imaging by Generalized-series Reconstruction
SD	Standard deviation
SNR	Signal-to-noise ratio
SVD	Singular value decomposition
T_1	Longitudinal relaxation time
T_2	Transverse relaxation time
T_E	Echo time
T_R	Repetition time
TRIGR	Two-reference RIGR

CHAPTER 1

INTRODUCTION

1.1 Problem Statement

This research is about dynamic magnetic resonance imaging (MRI). Although dynamic imaging may mean different things in different applications, from the data acquisition standpoint, it can always be characterized as the collection of a sequence of images $I_1(r)$, $I_2(r)$ ... $I_n(r)$. Sometimes, this type of experiment is termed time-sequential imaging. The interimage variations $\Delta I = I_n - I_{n-1}$ are commonly called dynamic changes. For this study, we assume that the dynamic changes may or may not be time-dependent *per se*. For example, in diffusion-weighted imaging, the dynamic changes do not reflect an underlying time variation in the object, but are due to manipulation of the data acquisition procedure as the image sequence progresses. On the other hand, the dynamic changes can relate to a time-dependent change in the object being imaged, such as that which occurs when using MRI to guide the insertion of a biopsy needle.

Dynamic MRI is becoming an increasingly important area of research due to the many practical applications. A particular example of interest is MR mammography in which a time-series of images of the breast is taken to monitor the wash-in/wash-out of an injected contrast agent. The interest in this lies in the possibility that the temporal shape of the enhancement curve, as well as the spatial pattern of enhancement in a lesion, can determine noninvasively whether a lesion is benign or malignant [1–9]. To capitalize on the period of greatest differentiation between malignant and benign lesions, a sequence of images must be acquired during the first 1 or 2 minutes following contrast injection [10,11], leading to the requirement of high temporal resolution.

In addition, high spatial resolution in three dimensions is imperative to allow the visualization of very small tumors with full coverage of the breast. A dynamic imaging method that could deliver simultaneously high temporal and spatial resolutions could detect cancerous lesions at an earlier stage, thus improving the patient's prognosis. Additionally, a method of noninvasive lesion characterization could reduce the physical and mental toll on the patient, as well as the financial cost. The ability to acquire rapid, high-quality images would also have application in contrast-enhanced imaging of other types of cancers for detection [12,13], monitoring the effects of treatment [14] and watching for recurrence [12].

The focus of this research is obtaining high spatial and temporal resolutions simultaneously. Specifically, we investigate how to obtain high-resolution image sequences with a reduced number of dynamic data. Practical issues related to motion, signal-to-noise ratio and resolution capability are also addressed in this dissertation.

1.2 Background

1.2.1 Signal expression

The signal activated from a sample (or a spin system) after a pulse excitation can be written in the following form [15]:

$$d(t) = \int_{-\infty}^{\infty} W(\vec{r}) M(\vec{r}) e^{-i\gamma\omega(\vec{r})t} d\vec{r}, \tag{1.1}$$

where $d(t)$ is the activated signal, $W(\vec{r})$ is a window function that represents the excitation sensitivity, $M(\vec{r})$ is the spatial distribution of spins in the object, γ is a proportionality constant and $\omega(\vec{r})$ is the frequency of the activated signal. Typically, $W(\vec{r})$ defines a planar slice of the object [16], but more sophisticated spatially selective excitation schemes are possible such as those used in non-Fourier encoding methods. Note that the received signal in Eq. (1.1) is the integral over the entire excited region of the object.

1.2.2 The issue of imaging time

In order to create an image from the activated signal, it is necessary to encode spatial information into the signal [17]. Frequency-encoding makes the frequency of the acquired signal depend on the location of the spins as

$$\Delta\omega(r_{fe}) = \gamma G_{fe} r_{fe}, \tag{1.2}$$

where $\Delta\omega(r_{fe})$ is the change in frequency as a function of position along the frequency-encoding direction and G_{fe} is the applied frequency-encoding gradient. The phase-encoding method encodes the spatial information into the initial phase of the received signal as

$$\phi(r_{pe}) = -\gamma G_{pe} r_{pe} T_{pe}, \tag{1.3}$$

where $\phi(r_{pe})$ is the phase as a function of position along the phase-encoding direction, G_{pe} is the applied phase-encoding gradient and T_{pe} is the phase-encoding time period. The encoding process can be described using the popular k-space notation [18] in which the k-space variable $\vec{k}$ is defined as

$$\vec{k}(t) = \int_0^t \frac{\gamma}{2\pi} \vec{G}(t) dt, \tag{1.4}$$

where $\vec{G}$ is the applied gradient magnetic field. Using this notation, the imaging equation is given by the Fourier transform as

$$d(\vec{k}) = \int_{-\infty}^{\infty} W(\vec{r}) I(\vec{r}) e^{-i2\pi\vec{r}\cdot\vec{k}} d\vec{r}, \tag{1.5}$$

where $d(\vec{k})$ is the acquired signal and $I(\vec{r})$ is the desired image function.

To create a good quality image, measurements must be made from many locations in k-space. In the conventional Fourier imaging technique, a combination of the phase and frequency-encoding methods discussed above is used. During each data acquisition period, a set of data points is acquired using frequency encoding as

$$k_{fe}(n) = \frac{\gamma}{2\pi} G_{fe} n \Delta t \qquad \frac{-N_{fe}}{2} \leq n \leq \frac{N_{fe}}{2}, \tag{1.6}$$

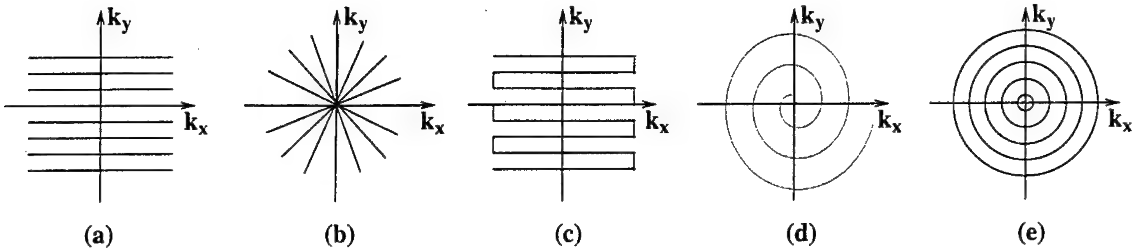

Figure 1.1: Coverage of k-Space: (a) standard Fourier encoding, (b) projection reconstruction, (c) echo planar and fast spin-echo, (d) spiral scanning and (e) concentric scanning.

where N_{fe} is the number of points acquired in the frequency-encoding direction and Δt is the time increment between samples. For the phase-encoding direction, the value of the phase-encoding gradient is incremented between each of the N_e encodings as

$$k_{pe}(n) = \frac{\gamma}{2\pi} n \Delta G_{pe} T_{pe} \qquad \frac{-N_e}{2} \leq n \leq \frac{N_e}{2}, \tag{1.7}$$

where ΔG_{pe} is the step in phase-encoding gradient. The resulting coverage of k-space is shown in Fig. 1.1(a). Another example is projection reconstruction imaging, which uses frequency encoding for two dimensions. In this case, k-space is covered in a radial fashion as shown in Fig. 1.1(b) by incrementing two frequency-encoding gradients as

$$k_{fe1}(n) = \frac{\gamma}{2\pi} G \cos(n\Delta\phi) t \qquad \text{and} \tag{1.8a}$$

$$k_{fe2}(n) = \frac{\gamma}{2\pi} G \sin(n\Delta\phi) t \qquad \frac{-N_e}{2} \leq n \leq \frac{N_e}{2}, \tag{1.8b}$$

where G is a constant and $\Delta\phi$ is the angular increment in k-space.

No matter what coverage of k-space is selected, the time to acquire an image depends upon the number of encodings that are required. If T_R is the repetition time or the time for one encoding and N_e excitations are necessary, the total imaging time will be

$$T = N_e T_R. \tag{1.9}$$

In many cases, the minimum value of T_R is limited by the T_1 tissue relaxation parameter in which case, an increase in temporal resolution would have to come through a reduction in the number of acquired encodings.

1.2.3 The issue of image resolution

Describing the MR imaging process in terms of linear system theory, the resulting image $\hat{I}(\vec{r})$ will be related to the original object $I(\vec{r})$ through a convolution as

$$\hat{I}(\vec{r}) = I(\vec{r}) * h(\vec{r}), \tag{1.10}$$

where $h(\vec{r})$ is the point spread function (PSF) of the imaging process. The width of the PSF defines the separation required between two points in the object such that they can be resolved in the image and thus, gives a measure of the spatial resolution of the image. The width of the PSF is often described in terms of the width w of an equivalent rectangle as

$$\int_{-\infty}^{\infty} h(0)\mathrm{rect}\left(\frac{r}{w}\right) dr = \int_{-\infty}^{\infty} h(r)dr, \tag{1.11}$$

where

$$\mathrm{rect}(r) = \begin{cases} 1 & |r| < \frac{1}{2} \\ 0 & \text{else.} \end{cases} \tag{1.12}$$

For example, if the standard Fourier imaging method is used, the PSF will be

$$h(r) = \Delta k \frac{\sin(\pi N_e \Delta k r)}{\sin(\pi \Delta k r)} e^{-i\pi\Delta k r}, \tag{1.13}$$

where N_e is the number of k-space data points and Δk is the step size in k-space. Therefore, the spatial resolution of the resulting image is

$$\Delta r = \frac{1}{N_e \Delta k}, \tag{1.14}$$

where Δr is the pixel size in the image. By comparing Eqs. (1.9) and (1.14), it can be seen that an improvement in the temporal resolution through a reduced number of phase encodings will be accompanied by a commensurate loss in spatial resolution for the conventional Fourier imaging technique.

1.2.4 Fast imaging

For many dynamic imaging applications, fast imaging techniques are necessary to provide adequate temporal resolution. It is clear from Eq. (1.9) that one can increase

the temporal resolution of a sequence of images by either shortening T_R or reducing N_e. Techniques that use the former strategy are called fast-scan techniques and the latter are called reduced-scan techniques.

Fast-scan imaging techniques try to acquire a full set of data in a time that is short compared to the dynamic process. The k-space coverage of several of these techniques is illustrated in Fig. 1.1(c)-(e). Echo planar [19,20] uses a rapidly switching frequency encoding gradient to cover k-space in a rectilinear fashion during data acquisition. The fast spin-echo technique [21–23] obtains the same k-space coverage as echo planar, but uses multiple refocussing pulses instead of the gradient switching. Because the data for these methods are acquired on a rectilinear grid, image reconstruction can be easily performed using the fast Fourier transform (FFT). Spiral scanning [24–26] applies time-varying frequency encoding gradients during data acquisition to traverse a spiral trajectory in k-space. Image reconstruction for spiral scanning requires interpolation to a Cartesian grid followed by the FFT [27,28]. With this reconstruction method, it is necessary to know the exact k-space location of the data points to avoid image artifacts, often necessitating the measurement of the actual k-space trajectory due to imperfect gradient performance [29,30]. Concentric scanning [31,32] also uses a modulated frequency encoding gradient, but acquires circles of data in k-space instead of a spiral of data. For all of these techniques, an image can be generated with a single excitation or interleaved segments of the required data can be acquired with a few excitations. Although fast-scan techniques are capable of acquiring an image in a short time, they may require specialized hardware for implementation. In addition, they may have reduced contrast between tissues and a reduced signal-to-noise ratio (SNR). For dynamic imaging applications, there may also be power deposition problems due to the multiple images that are acquired.

In contrast to the fast-scan methods, the reduced-scan methods try to improve the temporal resolution by reducing N_e. These techniques are motivated by the observation that in many dynamic imaging applications, the dynamic process induces a contrast modulation on the underlying static high-resolution morphology. They exploit this fact to reduce the redundancy in the data acquisition process to improve

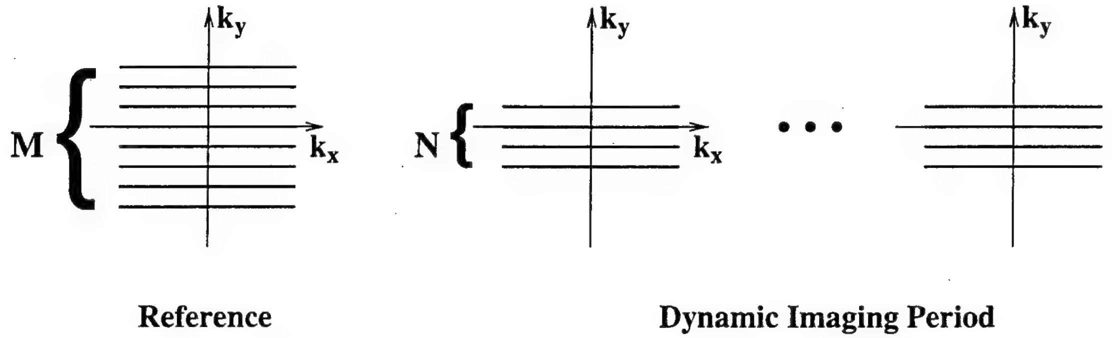

Figure 1.2: Reduced-Encoding Data Acquisition: A high-resolution reference data set is followed by a series of reduced-encoding data sets during the dynamic imaging period.

the temporal resolution. The reduced-scan data acquisition strategy is illustrated in Fig. 1.2. A high-resolution reference data set is acquired, followed by a sequence of reduced-encoding dynamic data sets. If M and N encodings are acquired for the reference and dynamic data sets, respectively, the improvement in temporal resolution for the dynamic images will be M/N. However, as discussed before, this will result in a loss of spatial resolution with the conventional Fourier reconstruction method. To avoid this loss of spatial resolution, many of the reduced-encoding dynamic imaging methods use *a priori* information from the reference image at some point in the imaging process to reduce the number of encodings required per dynamic image.

Several of the reduced-scan techniques, such as wavelet encoding methods [33–57] and singular value decomposition methods [58–70], use the *a priori* information during the data acquisition process to determine a more optimal truncated basis set than the infinite complex exponentials of the Fourier encoding set. The hope is that the non-Fourier basis vectors will be better able to encode the information in the object with a small number of basis functions. Other reduced-scan techniques use the *a priori* information as a constraint for extrapolation of the missing dynamic data during image reconstruction [71]. These include the reduced-encoding imaging by generalized-series reconstruction (RIGR) method [72, 73] and the keyhole or data-replacement technique (DRT) [74, 75]. The reduced-scan methods will be discussed in more detail in Chapter 2.

1.3 Summary of Results

The key issue addressed in this research is how to obtain simultaneously high spatial and temporal resolutions within the reduced-encoding dynamic imaging framework. To avoid the loss of spatial resolution that occurs with reduced-encoding Fourier imaging, many methods make use of *a priori* information to reduce the number of encodings that are necessary for the dynamic images. In this dissertation, it was determined that if the *a priori* information that is available is a reference image, direct use of this information to "optimize" data acquisition using the existing wavelet transform or singular value decomposition schemes can undermine the capability to detect new image features. Incorporation of the *a priori* information in the image reconstruction step is preferable. We have also shown that the generalized series (GS) model of the RIGR technique is a better way to combine the reference and dynamic data for image reconstruction than the keyhole method.

Several techniques are proposed in this dissertation to improve the GS basis functions by introducing dynamic information. The two-reference reduced-encoding imaging by generalized-series reconstruction (TRIGR) method suppresses background information through the use of a second high-resolution reference image. This allows the GS basis functions to more accurately represent the areas of dynamic change. A second technique injects information from the dynamic data into the GS basis functions as opposed to deriving them solely from the reference information. The resulting GS basis functions more closely resemble those that would be derived from the dynamic image itself. Finally, motion that occurs between the acquisition of the reference data set and the dynamic data sets can render the reference information useless as a constraint for image reconstruction. This is a difficult problem to address, because the dynamic changes may alter the appearance of the image significantly, posing problems for both navigator-based techniques and registration algorithms. The proposed method uses a similarity norm to accurately detect the motion, in spite of the contrast changes, and can significantly reduce motion artifacts in GS images.

1.4 Organization of the Dissertation

The remainder of the dissertation is organized as follows. Chapters 2 and 3 investigate issues involved in data acquisition and image reconstruction for reduced-encoding dynamic imaging. Chapter 4 formulates a method to use the additional information in a second high-resolution reference image to suppress the background information in the GS basis functions. Chapter 5 details a method to use the edge information from the reference image with the contrast information from the dynamic data to improve the resulting dynamic images. Chapter 6 introduces a motion detection scheme for reduced-encoding dynamic imaging applications. Chapter 7 contains suggestions for future work and the conclusions drawn from this research.

CHAPTER 2

DATA ACQUISITION

For convenience, we shall denote the MRI data in terms of an inner product as

$$d(n) = \langle I, e(n) \rangle \qquad n \in \mathcal{N}, \tag{2.1}$$

where $d(n)$ is the acquired data, I is the object function and $e(n)$ are the encoding vectors. For reduced-encoding dynamic imaging, the key issue is the selection of a truncated set of basis functions $e(n)$, $n \in \mathcal{N}_{\text{dyn}} \subset \mathcal{N}$, to best represent the dynamic image I. With the typical Fourier reduced-encoding scheme, *a priori* information is not used to select the truncated set of encoding vectors. If it is desired to inject *a priori* information into the data acquisition, two current methods for doing that are the wavelet and singular value decomposition (SVD) encoding methods. The wavelet encoding scheme uses the *a priori* information only to guide the truncation; whereas, the SVD method uses the information to both select and truncate the encoding vector set. For this research, the wavelet and SVD encoding methods were investigated in comparison to Fourier encoding for reduced-encoding dynamic imaging applications.

2.1 Fourier Encoding

With the Fourier encoding method, the encoding vectors are the Fourier basis set of infinite complex exponentials $e^{i2\pi kr}$, where k is a spatial frequency variable. Although it would be possible to adaptively truncate the Fourier encoding vectors that are acquired for an object, typically no *a priori* information is used in the Fourier-encoding data acquisition process. Given that no *a priori* information is available about the object, it is optimal to sample data from the center of k-space because of

the well-known fact that k-space data decays as $1/k$ for practical image functions. This scheme can also be motivated by the observation that the central k-space data contributes the bulk of the contrast information to the resulting image; whereas, data in the outer region of k-space largely represents the edge information. Therefore, with Fourier encoding, the reduced-encoding data set that is collected is described by

$$d(n\Delta k) = \int_{-\infty}^{\infty} I(r) e^{-i2\pi n\Delta kr} dr \qquad \frac{-N}{2} \leq n \leq \frac{N}{2} - 1. \tag{2.2}$$

2.2 Wavelet Encoding

In contrast to the infinite complex exponentials of the Fourier basis set, the wavelet basis functions are localized in both the frequency and spatial domains. The basis set is formed from dilations and translations of a scaling function ϕ, which extracts an approximation of the object function, and the associated wavelet φ, which extracts the details of the object function. To form a wavelet basis set, the ϕ must be continuously differentiable and must satisfy $|\phi(r)| = \mathcal{O}(r^{-2})$ and $|\phi'(r)| = \mathcal{O}(r^{-2})$ [76]. Alternatively, the wavelet function must satisfy the admissibility condition [77]

$$\int \mathcal{F}\{\varphi\}(k)\ |k|^{-1}\ dk\ <\ \infty. \tag{2.3}$$

The commonly used wavelets can be classified into two general categories: orthogonal and biorthogonal. An orthogonal wavelet transform requires two basis sets. For a J-level discrete dyadic orthogonal wavelet transform, the set of these functions can be expressed as

$$\begin{aligned} \phi_{-J,k}(r) &= \sqrt{2^{-J}}\, \phi\left(2^{-J}r - k\right) \qquad k = 1, 2 \ldots, M2^{-J} \qquad \text{and} && \text{(2.4a)} \\ \varphi_{j,l}(r) &= \sqrt{2^{j}}\, \varphi\left(2^{j}r - l\right) \qquad j = -1, -2 \ldots, -J; l = 1, 2 \ldots, M2^{j}, && \text{(2.4b)} \end{aligned}$$

where ϕ and φ are the scaling function and wavelet, respectively, and M is the number of points across the object function. The other category is biorthogonal wavelets, which have the advantage of linear phase. (It has been shown that traditional wavelets can only be orthogonal and linear phase simultaneously for the Haar

wavelet basis [77].) For biorthogonal wavelets, four basis sets are required because the analysis and synthesis scaling functions (wavelets) cannot be the same function as in the orthogonal case. For a J-level discrete dyadic biorthogonal wavelet transform, the set of these functions can be expressed as

$$\begin{aligned}
\phi_{-J,k}(r) &= \sqrt{2^{-J}}\,\phi\left(2^{-J}r-k\right) && k=1,2\ldots,M2^{-J}, && && (2.5a)\\
\varphi_{j,l}(r) &= \sqrt{2^{j}}\,\varphi\left(2^{j}r-l\right) && j=-1,-2\ldots,-J; l=1,2\ldots,M2^{j}, && && (2.5b)\\
\breve{\phi}_{-J,k}(r) &= \sqrt{2^{-J}}\,\breve{\phi}\left(2^{-J}r-k\right) && k=1,2\ldots,M2^{-J} && \text{and} && (2.5c)\\
\breve{\varphi}_{j,l}(r) &= \sqrt{2^{j}}\,\breve{\varphi}\left(2^{j}r-l\right) && j=-1,-2\ldots,-J; l=1,2\ldots,M2^{j}, && && (2.5d)
\end{aligned}$$

where ϕ and φ of Eq. (2.4) are the analysis scaling function and wavelet, respectively, and $\breve{\phi}$ and $\breve{\varphi}$ are the synthesis scaling function and wavelet, respectively. Note that the basis functions are down-sampled by a factor of two at each level due to the dilation, and hence, the transform will not have redundant information. Therefore, a signal of M samples can be represented by a J-level discrete wavelet transform of M total coefficients ($M2^{-J}$ scaling coefficients and $M\sum_{j=-1}^{-J}2^{j}$ wavelet coefficients).

By wavelet theory, the wavelet coefficients that are the largest are the most important, and these tend to be sparse, meaning that most object functions can be well represented with a truncated set of wavelet coefficients. To try to exploit this property for dynamic MRI applications, wavelet encoding is applied in the following way. First, a high-resolution reference image is collected, typically with Fourier encoding. This reference image is decomposed along the proposed wavelet encoding direction using the 1D wavelet transform. Based on a chosen criteria, the "most important" N wavelet basis functions are selected to be used as excitation profiles for the dynamic imaging period. This reduced set of encodings that is acquired can be expressed as, for a J-level wavelet transform,

$$\begin{aligned}
\hat{A}_{2^{-J}}\{I_{\text{dyn}}\} &= \left\langle I_{\text{dyn}}(r), 2^{-J}\phi\left(2^{-J}r-k\right)\right\rangle && k=k_1,k_2\ldots k_{N_\phi} && \text{and} && (2.6a)\\
\hat{D}_{2^{j}}\{I_{\text{dyn}}\} &= \left\langle I_{\text{dyn}}(r), 2^{j}\varphi\left(2^{j}r-l\right)\right\rangle && j=-1,-2\ldots-J; l=l_1,l_2\ldots l_{N_{\varphi,j}}, && && (2.6b)
\end{aligned}$$

where N_ϕ scaling functions and $N_{\varphi,j}$; $j = -1, -2\ldots, -J$ wavelets are utilized and $N = N_\phi + \sum_{j=-1}^{-J} N_{\varphi,j}$.

To perform wavelet encoding of an object, one must explicitly form the inner product of the object and the basis functions using spatially selective *RF* pulses to generate an excitation profile in the shape of the selected basis functions. In other words, the acquired signal is received from a scaling function or wavelet-shaped region of the object. The excitation profile is translated and dilated to acquire the set of data specified in Eq. (2.6). Translation of the excitation profile is accomplished by either shifting the center frequency of the *RF* pulse [40] or ramping the phase during the *RF* pulse [54]. Dilation of the excitation profile can be achieved by changing the gradient strength [40] or changing the length of the *RF* pulse [53].

2.3 Singular Value Decomposition Encoding

Another non-Fourier encoding method is based on the singular value decomposition (SVD). The SVD of a $j \times k$ matrix A of rank r is defined as

$$A = U\Sigma V^H, \tag{2.7}$$

where U and V are $j \times j$ and $k \times k$ unitary matrices, respectively, and Σ is a $j \times k$ diagonal matrix. The columns of U and V are called the left and right singular vectors, respectively, and the r diagonal entries of Σ are called the singular values. The SVD can also be written as

$$A = \sum_{i=1}^{r} \sigma_i \vec{u}_i \vec{v}_i^H, \tag{2.8}$$

where $\vec{u}_i$ and $\vec{v}_i$ are the columns of U and V, respectively, and σ_i are the diagonal entries of Σ.

With the SVD, it is easy to choose the optimal truncated encoding vector set using the Eckart and Young theorem [78]. This theorem states that the minimum distance in the L_2 norm sense between a matrix A of rank r and any matrix B of

rank less than or equal to $\hat{r} < r$ is achieved by the truncated SVD[1], which is defined as

$$\hat{A} = \sum_{i=1}^{\hat{r}} \sigma_i \vec{u}_i \vec{v}_i^H \tag{2.9a}$$

$$= U_{\hat{r}} \Sigma_{\hat{r}} V_{\hat{r}}^H. \tag{2.9b}$$

Here $\Sigma_{\hat{r}}$ is a diagonal matrix containing the $\hat{r}$-most significant singular values, and $U_{\hat{r}}$ and $V_{\hat{r}}$ are the matrices consisting of the left and right singular vectors, respectively, that are associated with the $\hat{r}$-most significant singular values.

This feature of the SVD has been exploited in many fields and is the basis for its application to dynamic MR imaging. The truncated SVD representation of a reference image is used to define the encoding vectors for the dynamic data acquisition, in the hopes that these vectors would also form a good representation for the dynamic image. Specifically, given a reference image I_{ref}, the singular value decomposition of the reference image is first performed as

$$I_{\text{ref}} = U \Sigma V^H. \tag{2.10}$$

For SVD encoding along the vertical or horizontal directions, the $\vec{u}_i$ or $\vec{v}_i$, respectively, corresponding to the largest N singular values are selected as the encoding vectors for the dynamic imaging period. In the pure vertical encoding case, for example, the dynamic data set generated for each dynamic image is the projection of the ideal image I_{dyn} onto the space spanned by the selected left singular vectors. This can be expressed mathematically as

$$S_{\text{dyn}} = U_N^H I_{\text{dyn}}, \tag{2.11}$$

where U_N is the matrix constructed from the N selected left singular vectors. As with wavelet encoding, SVD encoding requires that the inner product is explicitly created using spatially selective RF pulses to excite a region of the object in the shape of a selected SVD singular vector. Unlike wavelet encoding, which can use many translations and dilations of a given excitation profile depending upon the selected wavelet basis functions, each SVD encoding will involve a different excitation profile.

---

[1] Note that the minimizer of $||A - B||_2$ is unique if and only if $\sigma_{\hat{r}} > \sigma_{\hat{r}+1}$.

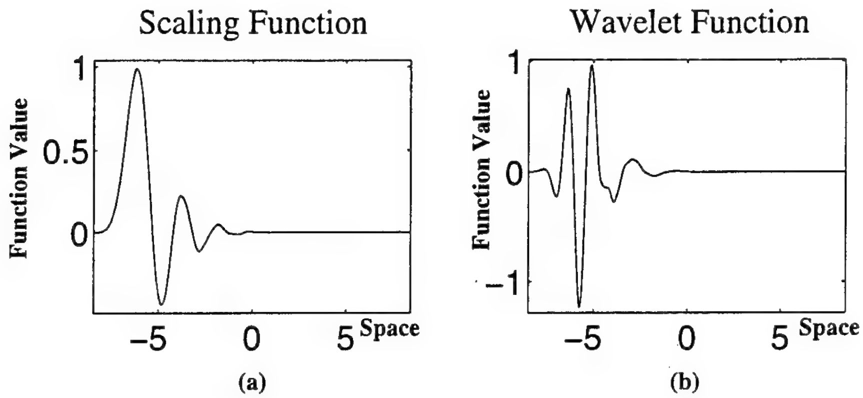

Figure 2.1: Daubechies D18 Orthogonal Wavelet: (a) scaling function and (b) wavelet

2.4 Encoding Method Assessment

The methods were compared using computer simulations on both simulated and real MRI data of dynamic imaging applications. To simulate the reduced phase-encoding data acquisition, k-space data sets were generated from a sequence of high-resolution images. A baseline high-resolution data set was used as the reference data, and the central N phase encodings from the remaining data sets were used as the dynamic phase encodings. To simulate wavelet encoding, the reference image was decomposed using the 1D wavelet transform. The N "most important" reference wavelet encodings were selected based on the squared sum along the frequency-encoding direction for each wavelet. The dynamic data associated with the selected wavelet encodings were generated using Eq. (2.6). To simulate the SVD encoding method, the singular value decomposition of the reference image was calculated, and the left singular vectors associated with the N largest singular values were selected as the dynamic encodings. The dynamic data were then generated using Eq. (2.11).

Note that with the wavelet encoding method, the choice of wavelet basis set will affect the results due to implementation issues, as well as the ability to represent the dynamic image with a truncated basis set. In selecting a particular wavelet basis set for experimental MR encoding, a smoother wavelet is preferred, because it requires

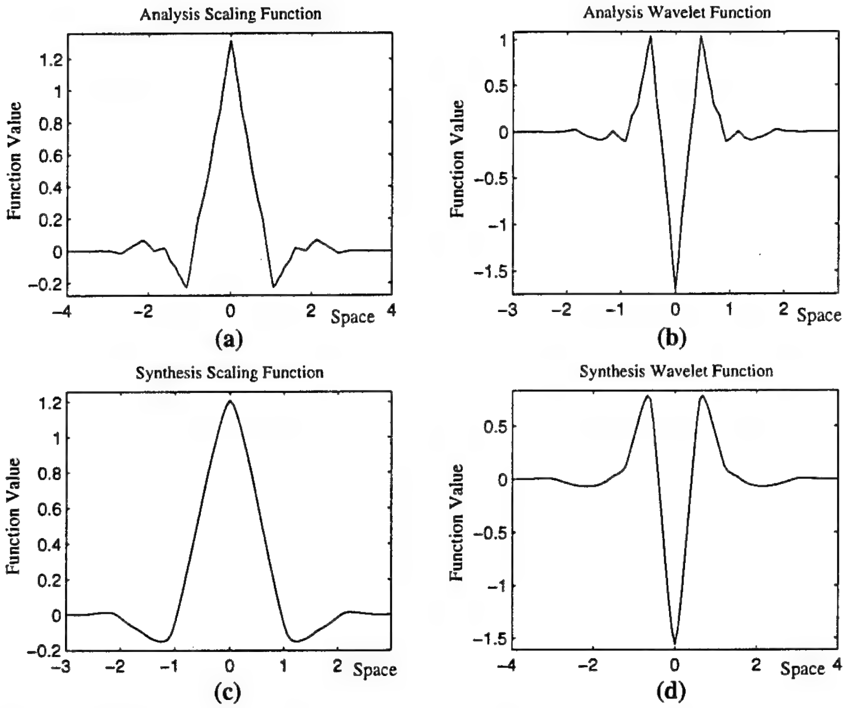

Figure 2.2: Cohen 7/9 Biorthogonal Wavelet: (a) analysis scaling function, (b) analysis wavelet, (c) synthesis scaling function and (d) synthesis wavelet

a shorter *RF* pulse [40] and reduces the bandwidth requirement of the *RF* pulse [52]. In addition, a more accurate wavelet-shaped profile can be excited, which will result in better images [40]. However, there is a trade-off between the length of the required *RF* pulse and the spatial support of the wavelet. This research utilized the orthogonal Daubechies D18 wavelet basis set [77] and the biorthogonal Cohen 7/9 wavelet basis set [79], pictured in Figs. 2.1 and 2.2, respectively, which are considered by many to be among the best for image compression [80]. This dissertation focused on the theoretical power of the basis set for encoding dynamic images and chose to ignore the long *RF* pulse that would be required to excite the profiles associated with these wavelets.

In addition, the non-Fourier encoding methods described here use the reference data set to choose the encoding vectors for the entire dynamic imaging period. A

modification of this technique is to use a reconstructed dynamic image to select the encodings for the subsequent dynamic image. Although this should help to increase the similarity between the image used to truncate the encoding vector set and the image acquired with the selected dynamic encodings, it would reduce the achievable temporal resolution due to the computation and magnet setup required between successive dynamic data sets.

It is important to note that the simulations in this study did not take into account several factors that would degrade the performance of the non-Fourier encoding methods. First, it was assumed that the spatially selective RF encodings could be exactly excited. This is difficult in practice, and imperfect excitation will degrade the resulting image [40,67]. In addition, T_1 variations across the image will further distort the encoded profile when a short T_R is used, which is especially a problem when a T_1 contrast agent is injected. The use of RF encoding with the non-Fourier methods also limits the application to single slice or 3D spin echo imaging, and it is not easy to implement 2D or thin slab 3D gradient echo sequences [61]. Another point is the signal-to-noise ratio (SNR) loss due to the use of spatially selective excitation for the non-Fourier encoding methods [40,47]. These problems do not arise with Fourier encoding, which uses linear gradients to encode the image information rather than spatially selective excitation.

As discussed earlier, the truncated wavelet and SVD representations have the desirable property of representing an image well with fewer encodings than are necessary with the Fourier encoding method. To exploit these desirable properties for reduced-encoding dynamic imaging, the current methods use a reference image to guide the truncation of the set of encoding vectors. The danger in doing that is that the selected encodings may not be optimal for the representation of the dynamic image and, at times, the reference-based truncation can introduce dangerous artifacts. To illustrate this, simulations of two important dynamic imaging applications, a contrast-enhanced dynamic study and an interventional MRI needle biopsy procedure, are shown below.

Figure 2.3 shows the results of a contrast-enhanced simulation in which the dynamic changes involve a variable rate of enhancement in each of the four "lesions,"

as well as a slow overall background enhancement. Figures 2.3(a)-(b) show the reference and dynamic images, respectively, reconstructed using 128 phase encodings. Figures 2.3(c)-(f) show the dynamic image reconstructed using 16 dynamic encodings using the Fourier, orthogonal wavelet, biorthogonal wavelet and SVD encoding methods, respectively. The SVD method results in a better delineation of the boundaries of the lesions than the other methods. However, it fails to faithfully reproduce the signal magnitudes in the lesions. This is quantified in Fig. 2.4 which shows the average signal magnitude in each of the lesions as assigned by the different methods. Note that the SVD methods assign nearly the same signal magnitude to all four lesions, which is undesirable because the aim of this application is to accurately track the signal magnitude change in the lesions.

In a needle biopsy application, the purpose of MR imaging is to accurately localize the needle to ensure that the lesion is biopsied as opposed to surrounding normal tissue. The results of a needle biopsy simulation are shown in Fig. 2.5 in which (a)-(b) are the reference and dynamic image, respectively, reconstructed using 256 phase encodings. The dynamic image contains an additional dark line feature, supposedly created by the insertion of a biopsy needle. The dynamic image is shown in (c)-(f), reconstructed using 32 dynamic encodings with the Fourier, orthogonal wavelet, biorthogonal wavelet and SVD encoding methods, respectively. Note the apparent displacement of the center of the needle in the SVD image and the smeared version of the needle in the wavelet reconstructions. In the Fourier image, the familiar Gibbs ringing results from the sharp edge features.

The smearing and displacement artifacts seen in the wavelet and SVD images are not due to the truncation level, but arise from the reference-based truncation method. To illustrate this, Figs. 2.6(a)-(c) were reconstructed using the optimal 32 orthogonal wavelet, biorthogonal wavelet and SVD encodings as determined by the dynamic image itself. The greatly improved reconstruction of the needle over that in Figs. 2.5(d)-(f) attest the nonoptimality of the dynamic encodings selected using the reference image of Fig. 2.5(a). However, note the bright needle ghost artifact in the orthogonal wavelet case, which occurs due to the localized nature of the wavelet basis functions.

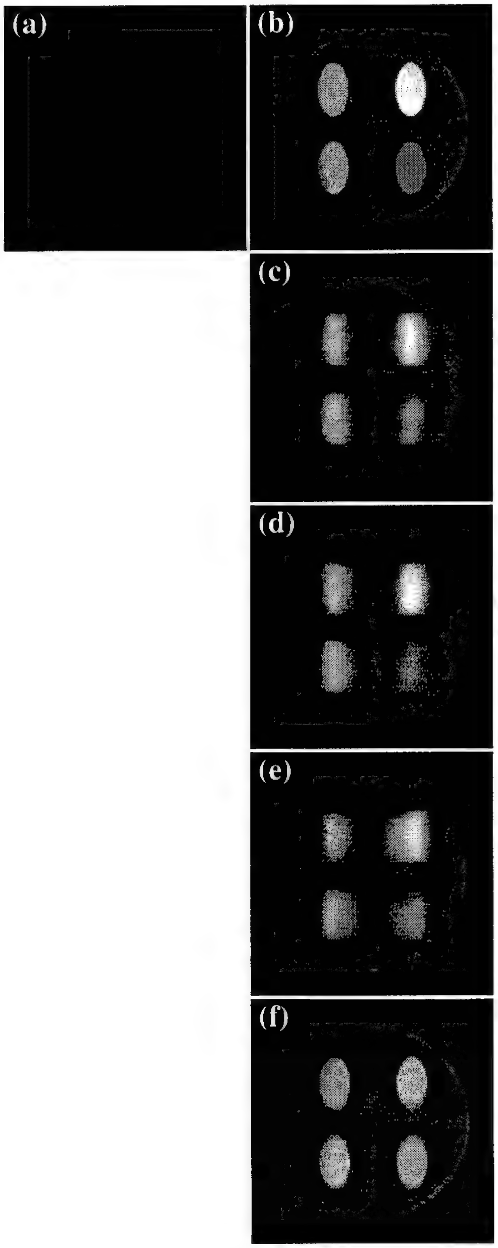

Figure 2.3: Non-Fourier Encoding Applied to Contrast-enhanced Imaging. (a)-(b) The reference and dynamic images, respectively, reconstructed using 128 phase encodings. The remaining images were reconstructed with 16 dynamic encodings using different encoding methods: (c) Fourier, (d) orthogonal wavelet, (e) biorthogonal wavelet, and (f) SVD. The Fourier, wavelet and SVD encoding directions are vertical. Note that the SVD method assigns nearly the same signal magnitude to all four lesions.

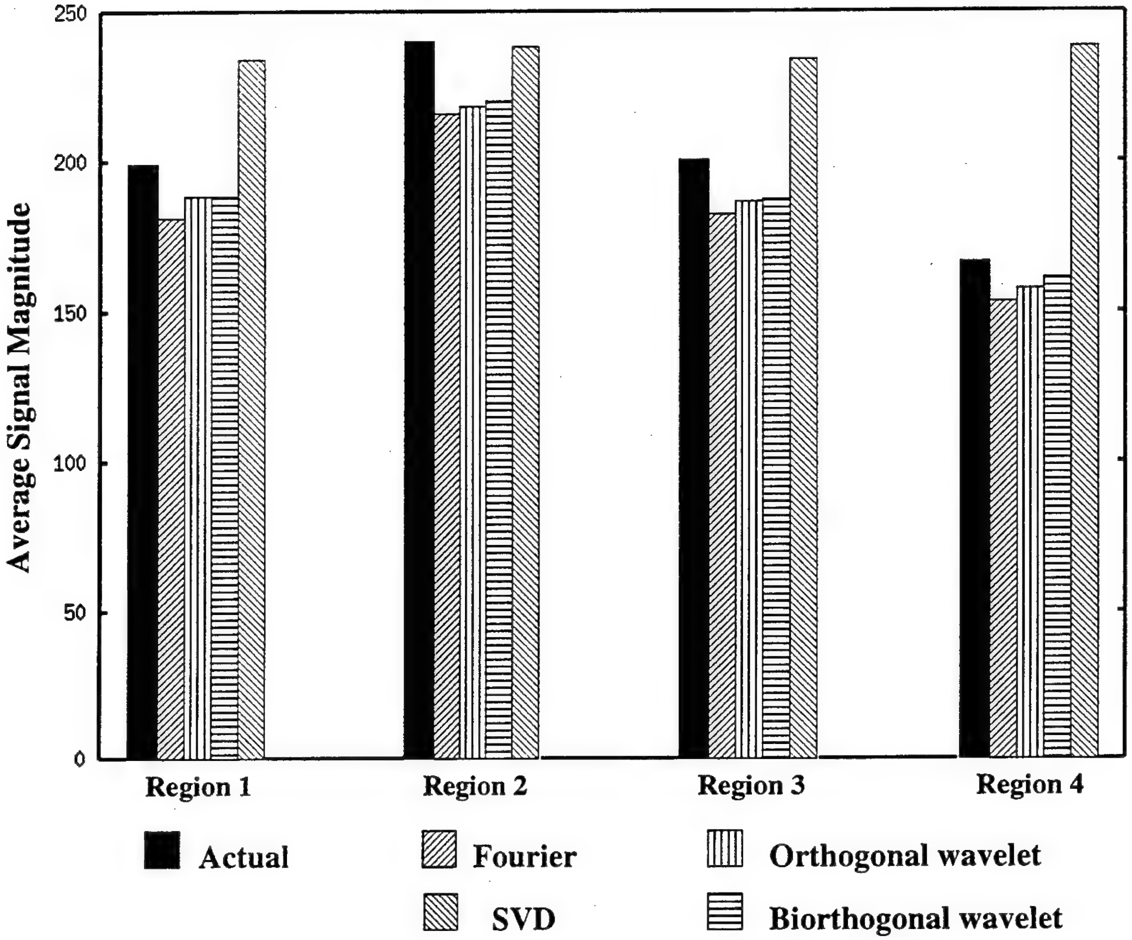

Figure 2.4: Average Signal Magnitude of the Lesions of Fig. 2.3(b)-(f). Regions 1-4 correspond to the upper-left, upper-right, lower-left and lower-right lesions, respectively, in Fig. 2.3.

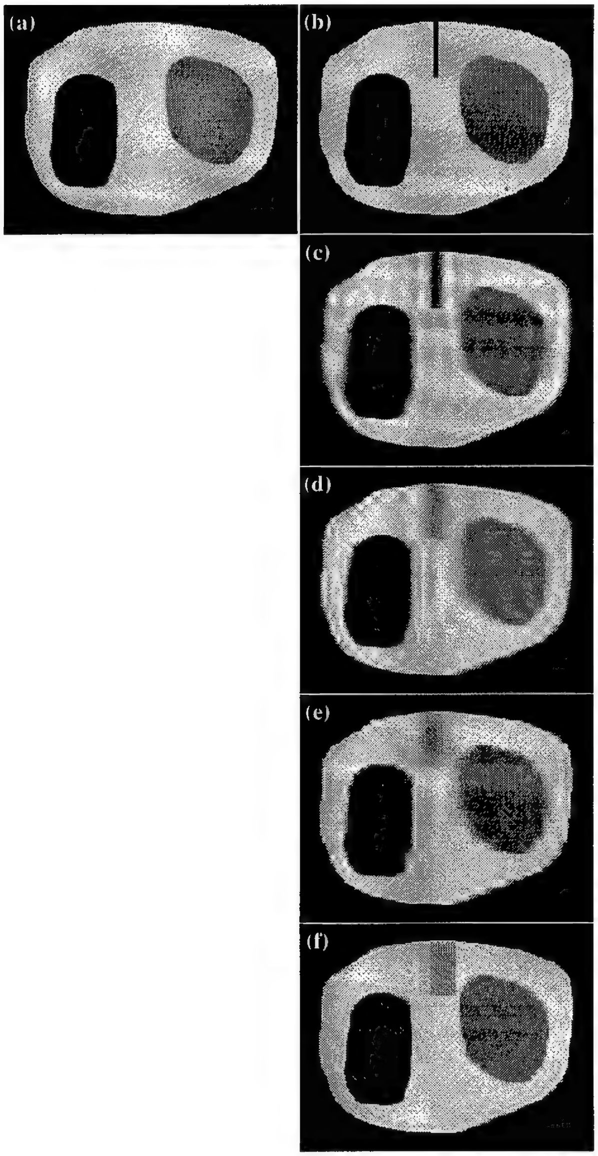

Figure 2.5: Non-Fourier Encoding Applied to Interventional MRI: (a)-(b) The reference and dynamic images, respectively, reconstructed using 256 phase encodings. The remaining images were reconstructed using 32 dynamic encodings with different encoding techniques: (c) Fourier, (d) orthogonal wavelet, (e) biorthogonal wavelet and (f) SVD. The Fourier, wavelet and SVD encoding directions are horizontal. The arrow indicates the center of the needle track. Note the apparent displacement of the needle center in the SVD reconstruction.

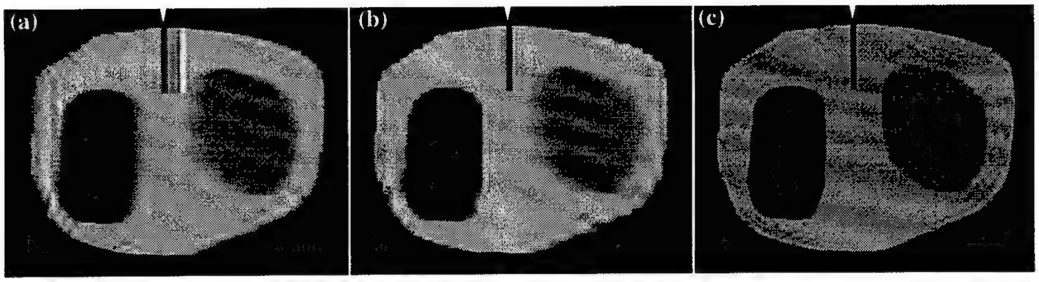

Figure 2.6: Optimal Non-Fourier Encoding: Dynamic image reconstructed with 32 optimal encodings as derived from the dynamic image itself using (a) orthogonal wavelet, (b) biorthogonal wavelet and (c) SVD. The wavelet and SVD encoding directions are horizontal, and the arrow indicates the center of the needle track. Note the improvement over the images in Fig. 2.5(d)-(f), respectively, which were reconstructed using the 32 sub-optimal encodings as determined from the reference image in Fig. 2.5(a).

2.5 Summary

The use of a reference image as the *a priori* information to guide the reduced-encoding data acquisition process does not achieve the goal of exploiting the desirable truncation properties of the non-Fourier basis sets and, at times, can create dangerous artifacts.

CHAPTER 3

IMAGE RECONSTRUCTION

The image reconstruction question is: given the available data,

$$d_{\text{dyn}}(n) = \langle I_{\text{dyn}}, e(n) \rangle \qquad n \in \mathcal{N}_{\text{dyn}}, \tag{3.1}$$

how can the original object function I_{dyn} be recovered? For the reduced-encoding case, the reconstructed object function is not unique, because there is not sufficient data available. In this case, *a priori* information can be used to help select a reconstruction from the set of possible choices. If *a priori* information is used, the key issue is how to effectively utilize it as a constraint during reconstruction [71] to recover the missing dynamic data $d_{\text{dyn}}(n), n \notin \mathcal{N}_{\text{dyn}}$. Three image reconstruction methods will be discussed in this section which use different strategies to handle the unmeasured dynamic data: zero-padded reconstruction, the data-replacement technique and the generalized-series method.

3.1 Zero-Padded Reconstruction

With the zero-padded reconstruction method, the unmeasured dynamic data are simply set to zero. More precisely, from the measured dynamic data $d_{\text{dyn}}(m), m \in \mathcal{N}_{\text{dyn}}$, a zero-padded data set is created as

$$\hat{d}_{\text{dyn}}(m) = \begin{cases} d_{\text{dyn}}(m) & m \in \mathcal{N}_{\text{dyn}} \\ 0 & \text{else,} \end{cases} \tag{3.2}$$

where the size of the resulting data set depends on the desired digital pixel size. This data set will then be processed with the conventional reconstruction method.

For example, with Fourier-encoded data, the image can be reconstructed using the discrete Fourier transform as

$$\hat{I}_{\text{dyn}}(n\Delta r) = \Delta k \sum_{m=-M/2}^{M/2-1} \hat{d}_{\text{dyn}}(m\Delta k) e^{i2\pi\frac{mn}{M}}, \tag{3.3}$$

where $\hat{d}_{\text{dyn}}$ is the zero-padded Fourier encoded data set and M is the size of the zero-padded data set. The discrete Fourier transform reconstruction can be efficiently performed using the Fast Fourier transform (FFT), which is one of the reasons for the popularity of the Fourier encoding method in MRI.

For orthogonal wavelet encoding, the original object can be reconstructed via the J level inverse wavelet transform as

$$I(r) = \sum_{k=1}^{M2^{-J}} \widehat{\mathcal{A}_{2^{-J}}}\{I\}\ 2^{-J}\phi(2^{-J}r - k) + \sum_{j=-1}^{-J} \sum_{l=1}^{M2^{-j}} \widehat{\mathcal{D}_{2^j}}\{I\}\ 2^j\varphi(2^j r - l), \tag{3.4}$$

where $\widehat{\mathcal{A}_{2^{-J}}}\{I\}$ is the zero-padded set of approximation coefficients and $\widehat{\mathcal{D}_{2^j}}\{I\}$ is the zero-padded set of wavelet coefficients. For biorthogonal wavelets, ϕ and φ in Eq. (3.4) will be replaced by $\breve{\phi}$ and $\breve{\varphi}$, respectively.

In the case of SVD encoding, the SVD synthesis procedure is used for image reconstruction. If the dynamic data were acquired using pure vertical SVD encoding as in Eq. (2.11), the synthesis equation is

$$\hat{I}_{\text{dyn}} = U\, \hat{S}_{\text{dyn}}, \tag{3.5}$$

where U is the matrix containing the full set of reference-left singular vectors and $\hat{S}_{\text{dyn}}$ is the zero-padded data matrix. To perform the zero-padding for this example, $M - N$ rows of zeros are appended to the bottom of the measured data matrix S_{dyn} of Eq. (2.11), where M and N are the number of SVD encodings measured for the reference and dynamic data sets, respectively. The zero-padding procedure can also be implicitly handled using the truncated SVD reconstruction procedure. For the pure vertical SVD encoding data set of Eq. (2.11), the measured data are multiplied by U_N as

$$\hat{I}_{\text{dyn}} = U_N\, S_{\text{dyn}}, \tag{3.6}$$

where U_N is the matrix constructed from the N-left singular vectors selected for the dynamic encoding.

3.2 Data-Replacement Technique

With zero-padded reconstruction, it is assumed that the unmeasured data is unimportant and can, therefore, be set to zero. For the keyhole or data-replacement technique (DRT) [74, 75], the underlying assumption is that the dynamic changes have a negligible effect on the unmeasured dynamic data points. With this assumption, the reference data can be used to directly substitute for the unmeasured dynamic data. If the measured dynamic data are $d_{\text{dyn}}(m), m \in \mathcal{N}_{\text{dyn}}$, and the reference data are $d_{\text{ref}}(m), m \in \mathcal{N}_{\text{ref}}$, a full data set is created by

$$\hat{d}_{\text{dyn}}(m) = \begin{cases} d_{\text{dyn}}(m) & m \in \mathcal{N}_{\text{dyn}} \\ d_{\text{ref}}(m) & m \in \mathcal{N}_{\text{ref}}, m \notin \mathcal{N}_{\text{dyn}}. \end{cases} \tag{3.7}$$

After the merged data set is created, the conventional image reconstruction procedure is used to reconstruct the dynamic image.

3.3 Generalized-Series Technique

Another method to incorporate *a priori* reference information into the reconstruction process is based on the generalized-series model. This method, called the reduced-encoding imaging by generalized-series reconstruction (RIGR) method [72,73], is useful for processing Fourier-encoded data. For wavelet and SVD-encoded data, there is no known better way to use the reference information in the reconstruction step than the keyhole method.

The generalized-series (GS) model can be described by

$$\hat{I}_{\text{dyn}}(r) = C(r) \sum_{n \in \mathcal{N}_{\text{dyn}}} c_n \, e^{i2\pi n \Delta k r}, \tag{3.8}$$

where $C(r)$ is the constraint function and Δk is the Fourier encoding step in k-space.

Therefore, the RIGR basis functions are the set of constrained exponentials

$$\varphi(r) = C(r)\, e^{i2\pi n \Delta k r}, \tag{3.9}$$

which contain *a priori* information from the constraint function. This results in a more rapidly convergent model than is possible with the infinite complex exponentials of the Fourier series. The specific form of the constraint function $C(r)$ depends upon whether or not a valid phase constraint is available [73]. If a valid phase constraint is not available, the model will be more stable if the phase is removed, resulting in basis functions of the form

$$\varphi(r) = |I_{\text{ref}}(r)|\, e^{i2\pi n \Delta k r}. \tag{3.10}$$

However, if a valid phase constraint is available, the dynamic changes will be better reproduced if the following basis functions are used

$$\varphi(r) = |I_{\text{ref}}(r)| e^{i\theta(r)}\, e^{i2\pi n \Delta k r}, \tag{3.11}$$

where $\theta(r)$ is the phase constraint.

During the extrapolation, data consistency between the reconstructed image and the measured dynamic data is enforced during the determination of the GS coefficients. If no phase is used, the data consistency constraint will force the GS parameters to absorb both the dynamic contrast changes and the phase variations. Therefore, it is desirable to have the sampling asymmetry small so that high-frequency phase variations will not introduce large asymmetric truncation artifacts. In this case, the N model parameters c_n must satisfy

$$d_{\text{dyn}}(m) = \sum_{n=-N/2}^{N/2-1} c_n\, \hat{d}_{\text{ref}}(m-n) \qquad -N/2 \leq m \leq N/2-1, \tag{3.12}$$

where symmetric sampling of k-space is assumed and

$$\hat{d}_{\text{ref}}(m-n) = \int_{-\infty}^{\infty} |I_{\text{ref}}(r)| e^{-i2\pi(m-n)\Delta k r} dr. \tag{3.13}$$

If phase constraints are used, the GS coefficients are forced to have Hermitian symmetry (i.e., $c_n = c^*_{-n}$), because the parameters need to model only the dynamic contrast

changes. Due to this forced Hermitian symmetry, the GS model can be symmetric irrespective of the symmetry of the sampled dynamic data, resulting in a higher order model and, therefore, reduced truncation artifacts. The result is two sets of linear equations that specify the GS parameters as

$$
\begin{aligned}
d_{\text{dyn}}(m) &= \sum_{n=-(N-N_0-1)}^{N-N_0-1} c_n \, d_{\text{ref}}(m-n) && \text{and} && (3.14\text{a}) \\
d^*_{\text{dyn}}(m) &= \sum_{n=-(N-N_0-1)}^{N-N_0-1} c_n \, d^*_{\text{ref}}(m-n) && -N_0 \leq m \leq N - N_0 - 1, && (3.14\text{b})
\end{aligned}
$$

where d_{ref} is the reference data. Because there are more equations than unknowns, this system should be solved in the least squares sense. Substituting the coefficients of Eq. (3.12) or (3.14) into the GS model will yield the desired dynamic image.

3.4 Generalized Point Spread Function

As discussed in Chapter 1, the width of the point spread function (PSF) gives a measure of the spatial resolution obtained from an imaging process. A common definition of the PSF width is the equivalent rectangle. Specifically, if $h(r)$ is the PSF, the width w of the equivalent rectangle is defined by

$$\int_{-\infty}^{\infty} h(0)\text{rect}\left(\frac{r}{w}\right) dr = \int_{-\infty}^{\infty} h(r) dr, \tag{3.15}$$

where

$$\text{rect}(r) = \begin{cases} 1 & |r| < \frac{1}{2} \\ 0 & \text{else.} \end{cases} \tag{3.16}$$

In the case of Fourier series reconstruction, the PSF is

$$h(r) = \Delta k \frac{\sin(\pi N_e \Delta k r)}{\sin(\pi \Delta k r)} e^{-i\pi\Delta k r}, \tag{3.17}$$

where N_e is the number of k-space data points and Δk is the step size in k-space, and the corresponding PSF width Δr is

$$\Delta r = \frac{1}{N_e \Delta k}. \tag{3.18}$$

Note that the width of the PSF for Fourier imaging depends only upon the number of encodings that are acquired, given a fixed k-space step size. On the other hand, for the case of constrained reconstruction methods and specifically for the case of GS reconstruction, the PSF width depends on both the number of encodings and the *a priori* information.

For this reason, a generalized PSF analysis was performed where the reference image was a boxcar function, and the dynamic change between the reference and dynamic images was a point change. The location of the point change was varied within the boxcar. It was either located in the center, shifted one-fourth of the width of the boxcar from the center, or shifted almost one-half (0.49) of the width of the boxcar from the center. The analysis was repeated for varying reference boxcar widths and a varying number of dynamic encodings.

Example profiles are shown in Fig. 3.1 for the case of eight dynamic encodings and a reference boxcar width of 0.03125 (FOV=1). To better show details of the plots, only the center fourth of the FOV is shown for each profile. Rows 1-3 depict the situation for a centered point change and a point change shifted one-fourth or one-half the width of the reference boxcar from the center, respectively. Figures 3.1(a)-(c) are the reference, dynamic and difference (point change) images, respectively, reconstructed using 512 phase encodings. Plots (d)-(e) show the point change reconstructed using the Fourier series and the generalized series, respectively. The reduced PSF width of the generalized series reconstruction when compared to the Fourier series is due to the fact that the generalized series basis functions contain information from the reference image, so they can more effectively reproduce the dynamic image for a given number of encodings than the infinite complex exponentials of the Fourier series. Note that in this case, the reference image contains no edge information for the new dynamic feature.

The effects of the reference boxcar width and number of dynamic encodings on the width of the PSF can be seen in Fig. 3.2. As would be expected, the width of the GS PSF decreases with an increasing number of dynamic encodings. This also holds true for the Fourier series reconstruction. Note also that the width of the GS PSF

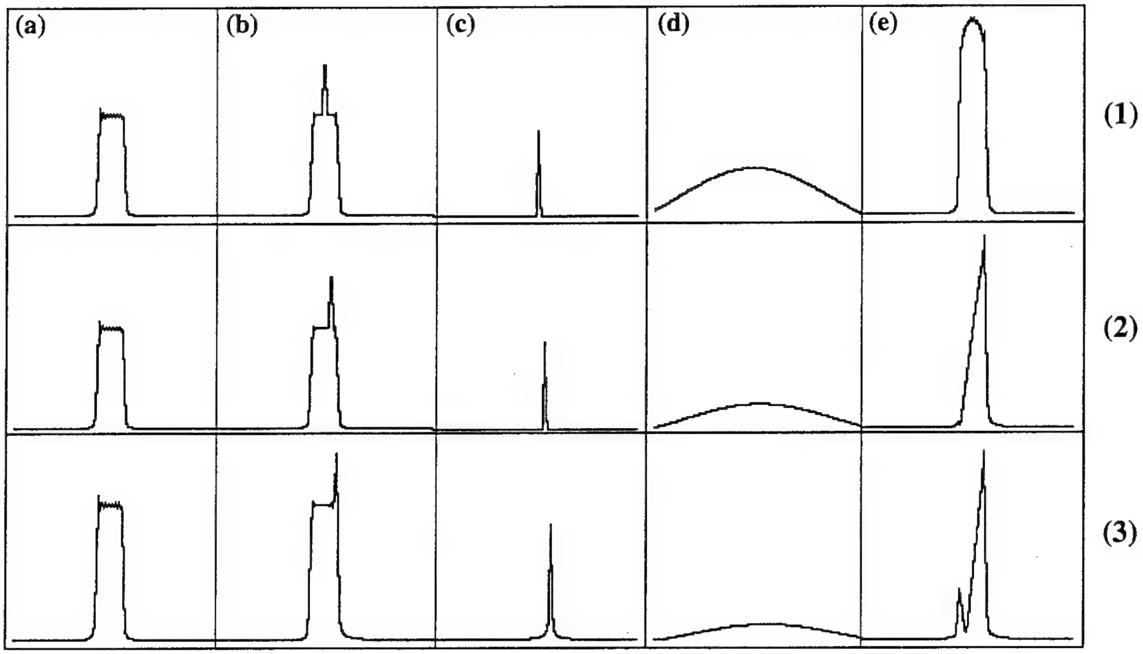

Figure 3.1: PSF Profiles I: Rows 1-3 show the PSF results for a delta function change that is centered in the reference boxcar, shifted by one-fourth the width of the reference boxcar, and shift by just under one-half (0.49) of the width of the reference boxcar, respectively. The width of the reference boxcar was 0.03125 (FOV=1), but only the center fourth of the plot is shown for better visualization. (a)-(c) The reference image, dynamic image and point change image (difference image), respectively, reconstructed using 512 phase encodings. (d)-(e) The point change reconstructed using the Fourier series and generalized series, respectively, using eight dynamic encodings. Note that (a)-(c) are on a different scale than (d)-(e).

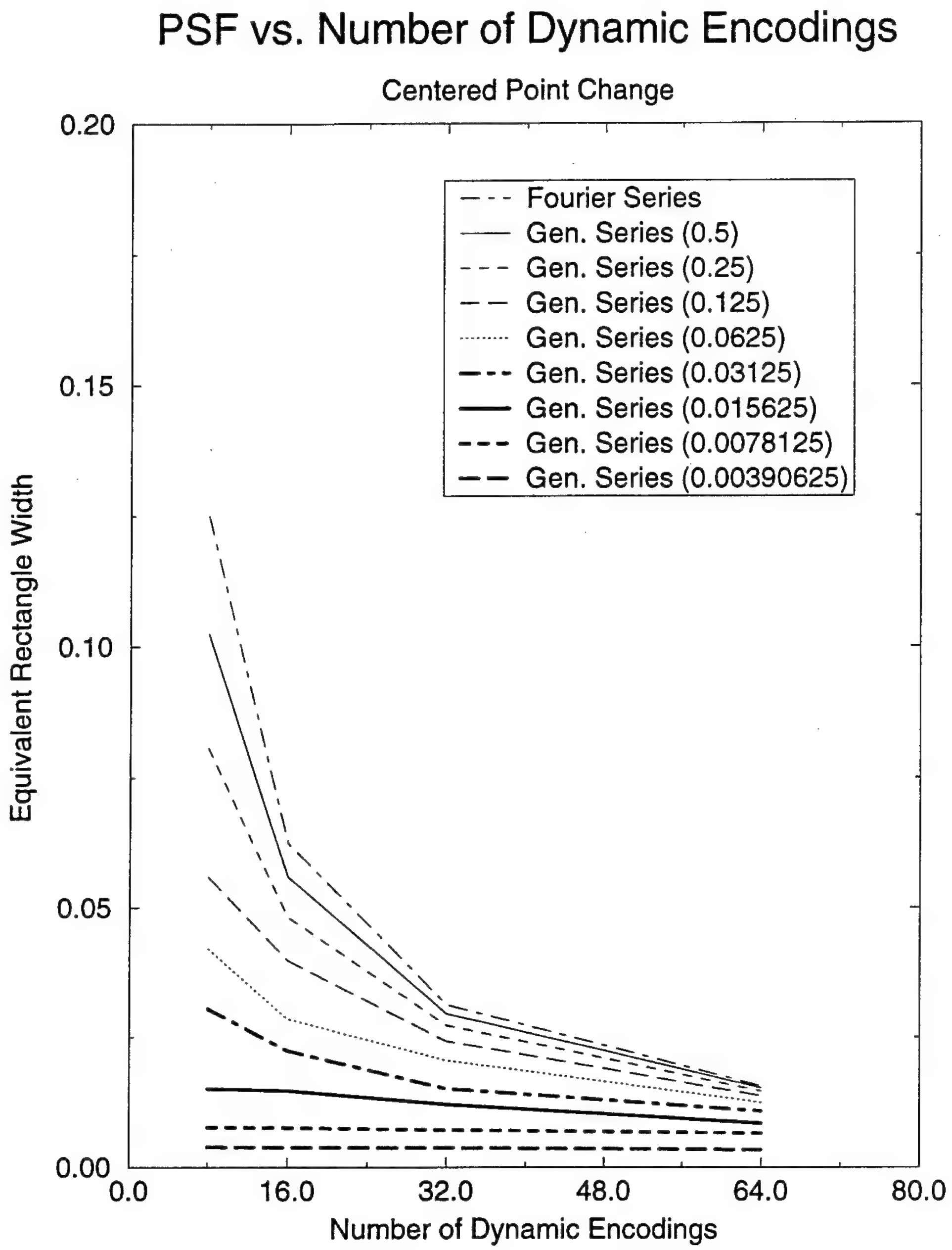

Figure 3.2: **PSF vs Number of Dynamic Encodings:** This plot shows the relationship of the width of the PSF versus the number of dynamic encodings used for the Fourier series and generalized series. In the simulations used to generate this plot, the point change was centered in the reference boxcar. Note the reduced PSF width of the GS as compared to the Fourier series for all reference boxcar widths and all numbers of dynamic encodings.

decreases for decreasing width of the reference boxcar. Although no additional direct information is available about the dynamic change, the reference information of the narrower boxcars is better able to constrain the reconstruction of the new dynamic feature. For every reference boxcar width, the width of the PSF is smaller for the generalized series than for the Fourier series. In the limit that the reference boxcar width equals the FOV, the generalized series has the same PSF width as the Fourier series. In fact, for this case of no effective *a priori* knowledge, the generalized series reduces to the Fourier series. This is desirable, because in the case of no *a priori* knowledge, the Fourier series would be the optimal reconstruction method (in the least squares sense).

The GS PSF width depends not only on the reference boxcar width, but also on the proximity of the point change to the nearest edge. This is illustrated in Fig. 3.3, which shows the PSF width as a function of the width of the reference boxcar for the Fourier series and the generalized series with various locations of the point change. Note that the PSF width of the generalized series decreases with increased proximity to an edge of the reference boxcar (i.e., increasing shift from the center). This occurs because the closer edge enables the GS basis functions to more effectively constrain the dynamic change reconstruction.

If the high-resolution reference image contains edge information for the dynamic feature, the GS PSF will be further improved as illustrated in Fig. 3.4. As before, rows 1-3 show the reconstruction of a dynamic point change that is centered in the reference boxcar and shifted one-fourth or approximately one-half (0.49) the width of the reference boxcar from the center, respectively. Figures 3.4(a)-(d) show the baseline reference image, the active reference image, the dynamic image, and the point change image (difference between the dynamic image and the baseline reference image), respectively, reconstructed using 512 phase encodings. Plot (e) shows the reconstruction of the point change obtained using the GS model with the active reference image and eight dynamic encodings. It is easy to see the improved PSF by comparison to the corresponding rows of Fig. 3.1(e).

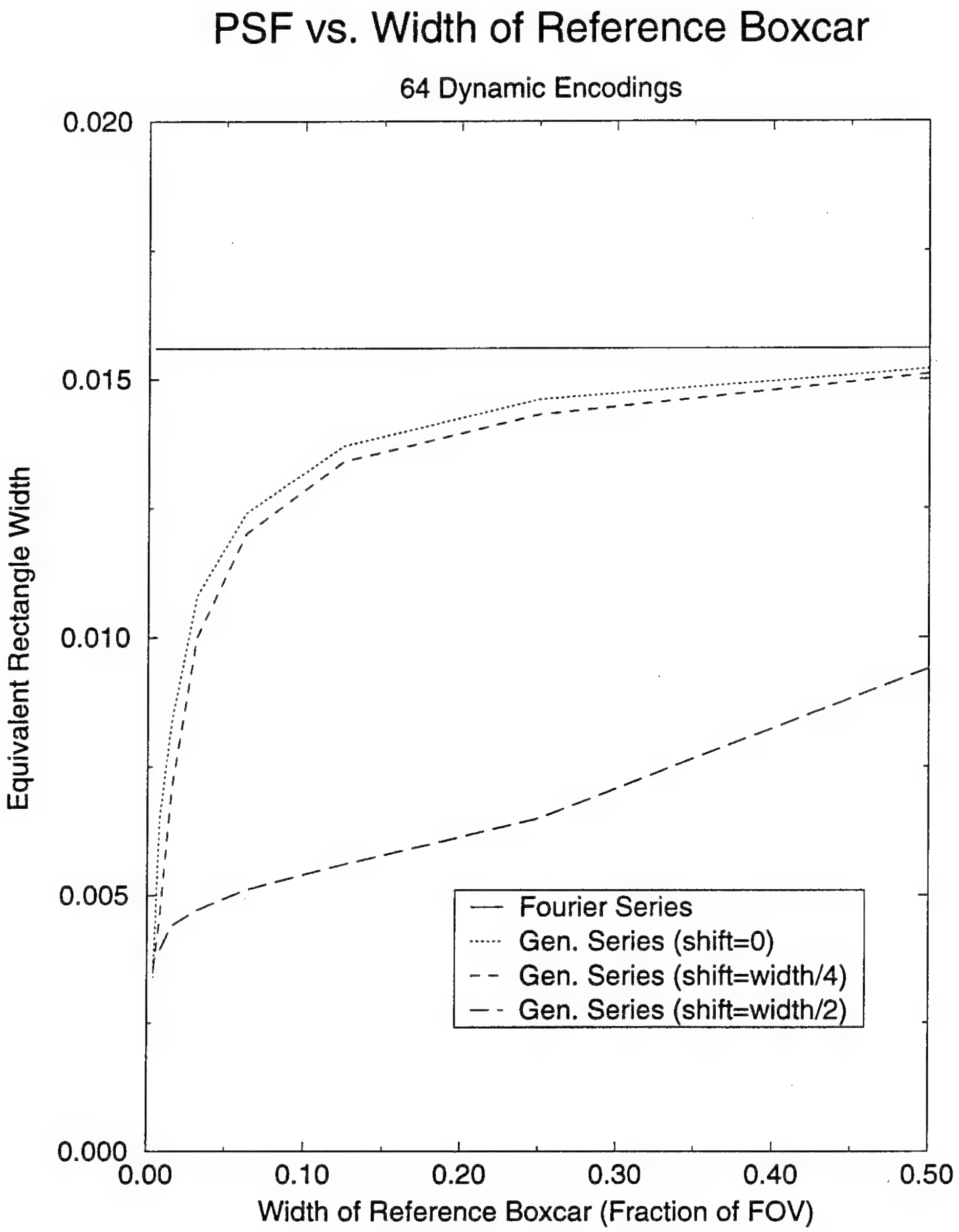

Figure 3.3: PSF vs Width of Reference Boxcar: This plot shows the relationship between the width of the PSF and the width of the reference boxcar for the Fourier series and generalized series for three locations of the point change. The simulations to generate this plot used 64 dynamic encodings.

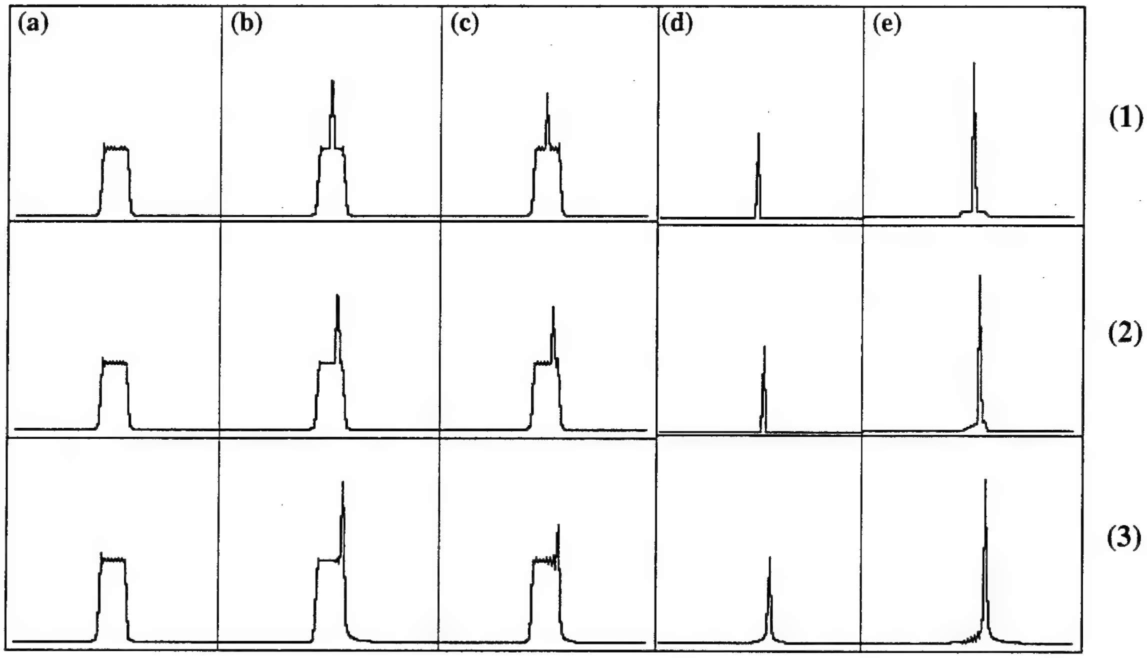

Figure 3.4: PSF Profiles II: Rows 1-3 show the PSF results for a delta function change that is centered in the reference boxcar, shifted by one-fourth the width of the reference boxcar, and shift by just under one-half (0.49) of the width of the reference boxcar, respectively. The width of the reference boxcar was 0.03125 (FOV=1), but only the center fourth of the plot is shown for better visualization. (a)-(d) The baseline reference image, the active reference image, the dynamic image, and the point change image, respectively, reconstructed using 512 phase encodings. (e) The point change reconstructed using the GS model with the active reference image and eight dynamic encodings. Note that (a)-(c) are on a different scale than (d)-(e).

In summary, the GS model has a smaller PSF width than the Fourier series even if the reference image contains no edge information for the dynamic feature because nearby edges help constrain the reconstruction of the dynamic feature. If the reference image does contain edge information about the dynamic feature, the PSF width will be further reduced.

3.5 Discussion

For image reconstruction, the use of *a priori* information in the constrained reconstruction techniques such as keyhole and RIGR can improve the resulting image appearance over that obtained through simple zero-padded reconstruction. However, the actual improvement gained will vary greatly depending upon the method of utilizing the *a priori* information. Although the keyhole method has been applied to reduced-encoding dynamic imaging applications due to its simplicity [67, 81, 82], it is important to note that the Fourier-keyhole method can only track the dynamic changes at the low resolution of $1/N\Delta k$, where N is the number of reduced dynamic encodings[1] [81, 83, 84]. This occurs because the keyhole method has the same PSF as the zero-padded Fourier series for reconstructing the dynamic changes. This can easily be seen as

$$
\begin{aligned}
I_{\text{diff}}(r) &= \hat{I}_{\text{dyn}}(r) - I_{\text{ref}}(r) && \text{(3.19a)} \\
&= \left\{ \sum_{n \notin \mathcal{N}_{\text{dyn}}} d_{\text{ref}}(n) e^{-i2\pi n \Delta k r} + \sum_{n \in \mathcal{N}_{\text{dyn}}} d_{\text{dyn}}(n) e^{-i2\pi n \Delta k r} \right\} && \text{(3.19b)} \\
&\quad - \left\{ \sum_{n} d_{\text{ref}}(n) e^{-i2\pi n \Delta k r} \right\} && \text{(3.19c)} \\
&= \sum_{n \in \mathcal{N}_{\text{dyn}}} \left\{ d_{\text{dyn}}(n) - d_{\text{ref}}(n) \right\} e^{-i2\pi n \Delta k r}. && \text{(3.19d)}
\end{aligned}
$$

On the other hand, the spatial resolution of the RIGR image depends upon both the dynamic and reference data sets. If well-defined boundaries for the feature exist in the reference image, it will be reconstructed with the spatial resolution of the reference

---

[1] For the wavelet-keyhole and SVD-keyhole methods, the resolution at which the dynamic changes can be followed will depend on the relationship between the dynamic changes and the selected wavelet or SVD encoding profiles.

image $1/M\Delta k$, where M is the number of reference encodings [73]. However, as was shown in the previous section, even if the dynamic changes introduce new edges to the image, the spatial resolution of these features can be improved over $1/N\Delta k$, because nearby edges in the reference image help to constrain the reconstruction of the new features. Therefore, with the same number of dynamic encodings, RIGR can reconstruct the dynamic changes with a greater spatial resolution than is possible with Fourier-keyhole. The effect of this can be seen in Fig. 3.5 in which (a)-(b) are the reference and dynamic images, respectively, reconstructed using 256 phase encodings. Figure 3.5(c) is the difference between these two images, effectively an image of the dynamic changes. Figures 3.5(d)-(e) show the difference image reconstructed with 32 dynamic encodings using Fourier-keyhole (or, equivalently, zero-padded Fourier series) and RIGR, respectively. Note that the RIGR method follows the dynamic changes at a much higher resolution than Fourier-keyhole.

In addition, image artifacts can arise due to data inconsistency between the reference and dynamic data sets with the keyhole method [85,86]. In the keyhole method where the reference data are simply pasted on the dynamic data, there is no guarantee of consistency between the reference and dynamic data sets. This can lead to image artifacts. In contrast, the unmeasured high-frequency dynamic data extrapolated using the GS model are $(N-1)^{th}$ order continuous with the measured dynamic data [73]. This leads to reduced artifacts in the reconstructed dynamic image. This is illustrated in Fig. 3.6 in which (a)-(b) are the reference and dynamic images, respectively, reconstructed with 128 phase encodings. Images (c)-(d) show the dynamic image reconstructed with 16 dynamic encodings using the Fourier-keyhole and RIGR methods, respectively. Note the data inconsistency artifacts in the Fourier-keyhole image, which are equivalent to a high-pass filtered version of the reference image.[2] On the other hand, the RIGR method can handle the data inconsistency between the reference and dynamic data sets due to the GS model-based extrapolation.

---

[2] Data inconsistency artifacts will also arise with the wavelet-keyhole and SVD-keyhole reconstruction methods, although the appearance of the artifacts will differ from those of the Fourier-keyhole method.

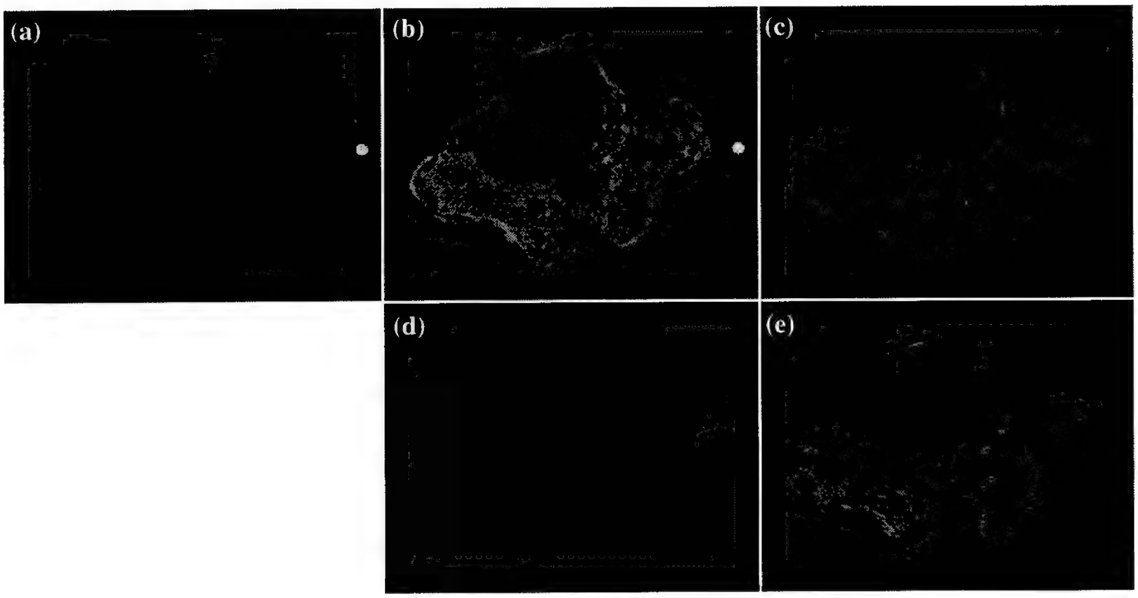

Figure 3.5: Dynamic Change Images: (a)-(c) The reference and dynamic images and the difference between the two, respectively. (d)-(e) The difference image reconstructed using 32 dynamic encodings with Fourier-keyhole (or, equivalently, zero-padded Fourier series) and RIGR, respectively. Note the improved reconstruction of the dynamic changes with the RIGR method.

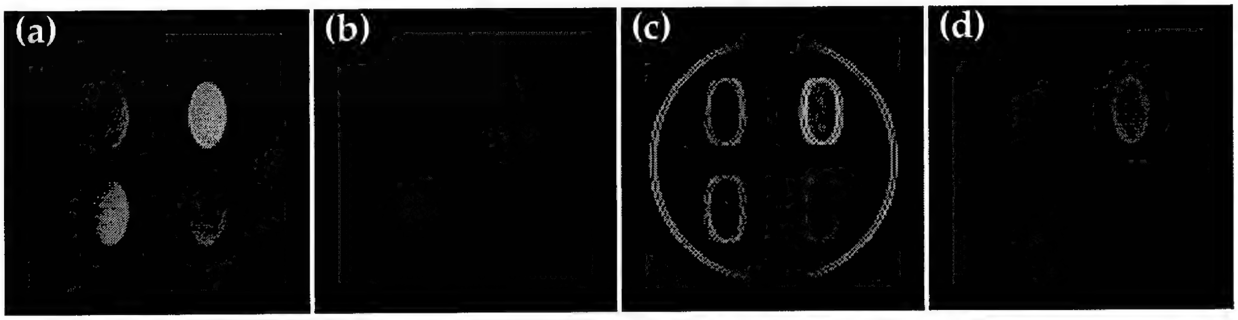

Figure 3.6: Keyhole Data Inconsistency Artifact: (a)-(b) The reference and dynamic images, respectively, reconstructed using 128 phase encodings. (c)-(d) The dynamic image reconstructed with 16 dynamic encodings using Fourier-keyhole and RIGR, respectively. The phase encoding direction is horizontal. Note the edge artifacts that appear in the Fourier-keyhole image.

3.6 Summary

If the *a priori* information that is available is a reference image, it is better used in the image reconstruction process than the data-acquisition step. For image reconstruction with Fourier encoding, the RIGR method is the best way to extrapolate the unmeasured data using the *a priori* constraints due to the higher resolution tracking of the dynamic changes and the reduced data inconsistency artifacts.

CHAPTER 4

TWO-REFERENCE RIGR

With the Fourier series, the spatial resolution of the reconstructed image depends solely upon the number of terms used in the series. On the other hand, the spatial resolution obtained with the generalized series (GS) model depends on both the number of terms and the GS basis functions. Due to the limited number of terms in the GS model, it would be better if only the areas of change were represented in the GS basis functions. The proposed two-reference reduced-encoding imaging by generalized-series reconstruction (TRIGR) method [87, 88] tries to achieve this by suppressing the background information in the GS basis functions through the use of a second high-resolution active reference image.

The motivation behind the research presented here is the consideration that, in some dynamic imaging applications, the dynamic process may change the appearance of parts of the image, while other parts remain relatively unchanged. For example, in contrast-enhanced dynamic imaging of breast cancer, where the aim is to track the changes that occur in the breast for several minutes following the injection of a contrast agent, the contrast between the tumor and the normal tissue may change drastically over the dynamic imaging period. The TRIGR method is well-suited for this application, because a second high-resolution reference image can be acquired following the dynamic imaging period when the contrast agent is strongly visible in the image. The second reference image can be used to suppress the background information in the generalized-series basis functions, thus improving the reconstructed dynamic image.

4.1 Two-Reference RIGR

Data acquisition for the proposed method is similar to the original RIGR method. A high-resolution baseline reference data set is acquired where the number of phase encodings is chosen to satisfy the spatial resolution requirements. This is followed by the acquisition of a series of reduced-encoding dynamic data sets where the number of Fourier encodings per set is chosen to give the desired temporal resolution. The high-resolution active reference data set is typically acquired at the end of the dynamic imaging period, although for some applications it may be desirable to place it at another point in the experimental procedure.

The proposed method suppresses background information in the GS basis functions through the use of a difference reference image which is created as

$$\tilde{I}_{\text{ref}} = \mathcal{F}\{\tilde{d}_{\text{ref}}\} = \mathcal{F}\{d_{\text{active}} - d_{\text{baseline}}\}, \tag{4.1}$$

where d_{active} and d_{baseline} are the high-resolution active and baseline reference data sets, respectively. The GS basis functions become the set of constrained exponentials $\tilde{I}_{\text{ref}} e^{i2\pi n\Delta kr}$, resulting in the model

$$I_{\text{diff}}(r) = \tilde{I}_{\text{ref}}(r) \sum_{n=-N/2}^{N/2-1} c_n e^{i2\pi n\Delta kr}, \tag{4.2}$$

where N is the number of dynamic encodings and symmetric k-space sampling has been assumed. Note that the TRIGR method directly reconstructs an image of the dynamic change. As such, the difference between the reduced dynamic encodings and the corresponding baseline reference encodings are used to determine the GS model coefficients. Specifically, the GS model coefficients c_n are obtained through a fitting step to maintain data consistency as

$$d_{\text{diff}}(m) = \sum_{n=-N/2}^{N/2-1} c_n \tilde{d}_{\text{ref}}(m-n), \tag{4.3}$$

where the dynamic difference data are obtained by subtracting from the dynamic data the corresponding encodings of the baseline reference image as

$$d_{\text{diff}}(n\Delta k) = d_{\text{dyn}}(n\Delta k) - d_{\text{baseline}}(n\Delta k) \qquad \frac{-N}{2} \le n \le \frac{N}{2} - 1. \tag{4.4}$$

Plugging these coefficients into Eq. (4.2) will yield the reconstructed dynamic change image. If the dynamic image itself is desired, it can be generated by adding the complex dynamic change image to the baseline reference image as

$$I_{\text{dyn}}(r) = I_{\text{baseline}}(r) \quad + \quad I_{\text{diff}}(r), \tag{4.5}$$

where $I_{\text{baseline}}(r)$ is reconstructed from $d_{\text{baseline}}(n\Delta k)$ using the standard Fourier technique.

The background information suppression achieved with this technique can result in significant improvement in the generalized PSF, as illustrated in Fig. 4.1. As before, rows 1-3 show the reconstruction of a dynamic point change that is centered in the reference boxcar and shifted one-fourth or approximately one-half (0.49) the width of the reference boxcar from the center, respectively. Figures 4.1(a)-(d) show the baseline reference image, the active reference image, the dynamic image, and the point change image (difference between the dynamic image and the baseline reference image), respectively, reconstructed using 512 phase encodings. Plot (e) shows the reconstruction obtained using the GS model with the difference reference image (active - baseline) and eight dynamic encodings. It is easy to see the improvement in the PSF due to the suppression of the background information in the difference reference image by comparison to the corresponding rows of Fig. 3.4(e). Although the case shown in Fig. 3.4 has the same amount of edge information for the dynamic feature, the background suppression provides additional improvement. Of course, this is the ideal case of complete background suppression. As the background information is less completely suppressed, the improvement seen with the TRIGR method will not be as great.

One could consider employing a similar methodology with the keyhole constrained reconstruction method by appending the high-frequency difference reference data to the low-frequency dynamic difference data sets followed by the inverse Fourier transform. Although the resulting dynamic images will be high-resolution, it is easy to prove that the actual dynamic signal changes will still be reconstructed with low-resolution. This behavior is similar to the single-reference image case analyzed by

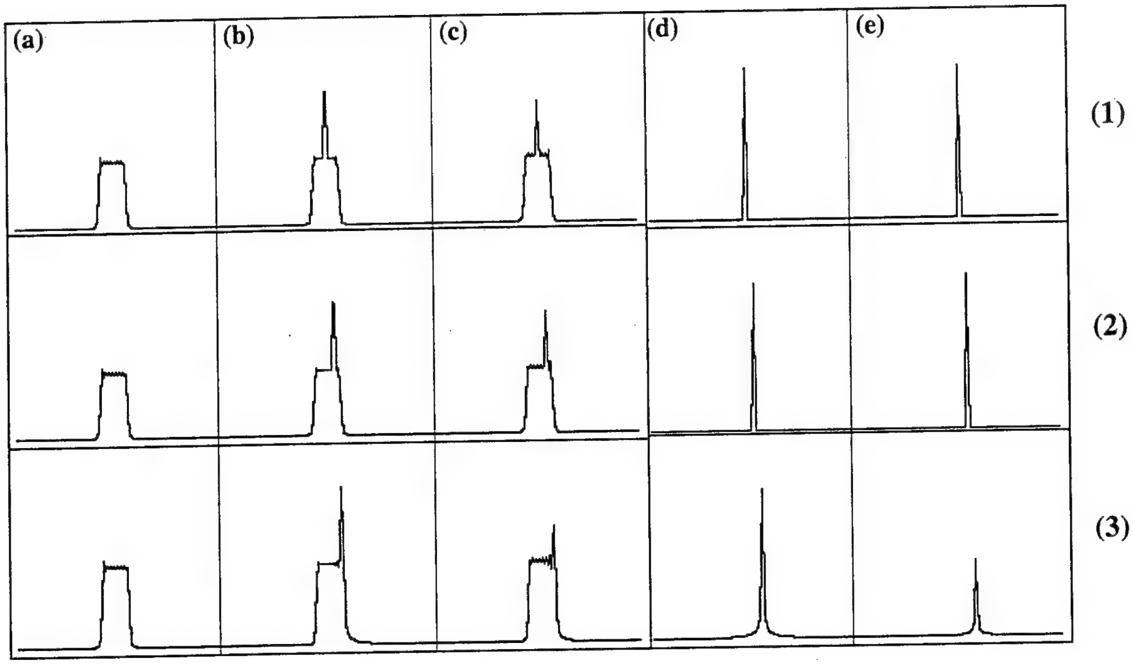

Figure 4.1: PSF Profiles III: Rows 1-3 show the PSF results for a delta function change that is centered in the reference boxcar, shifted by one-fourth the width of the reference boxcar, and shift by just under one-half (0.49) of the width of the reference boxcar, respectively. The width of the reference boxcar was 0.03125 (FOV=1), but only the center fourth of the plot is shown for better visualization. (a)-(d) The baseline reference image, the active reference image, the dynamic image, and the point change image, respectively, reconstructed using 512 phase encodings. (e) The point change reconstructed using the GS model with the a difference reference image (active-baseline) and eight dynamic encodings. Note that (a)-(c) are on a different scale than (d)-(e).

Spraggins [84] and Hu [83]; that is, no benefit is gained from the use of two-reference images in this keyhole scheme.

4.2 Results and Discussion

The proposed method was compared to the zero-padded Fourier transform and the original RIGR method using computer simulations. From a sequence of high-resolution data sets, baseline and active reference data sets were chosen. The central N encodings of the remaining data sets were used as the dynamic data sets, and the dynamic image was reconstructed with the three methods. The high-resolution dynamic image was reconstructed for comparison.

As mentioned before, the improvement of the proposed technique over the original RIGR method depends upon the degree of background suppression. The ideal case is if the difference image completely suppresses the background information. This case is illustrated in Figs. 4.2 rows 1-3 which show the resulting images and profiles through the upper and lower set of lesions, respectively, for a contrast-enhanced simulation in which the background tissue is completely suppressed in the difference reference image. In these figures, (a)-(c) are the precontrast reference, postcontrast reference and dynamic images, respectively, reconstructed using 128 phase encodings. Images (d)-(e) were reconstructed using RIGR with 16 dynamic encodings and the precontrast or postcontrast reference image, respectively. Image (f) was reconstructed using 16 dynamic encodings with the proposed method. The TRIGR method results in an improved reconstruction of the dynamic image because the GS basis functions need only represent the dynamic changes.

As the difference reference image suppresses the background less effectively, the performance improvement with the proposed method decreases. This is demonstrated in Fig. 4.3 rows 1-3 which show the images and profiles through the upper and lower set of lesions, respectively, resulting from a simulation in which the background tissue is not suppressed completely in the difference reference image. Figures 4.3(a)-(c) are the precontrast reference, postcontrast reference and dynamic images, respectively,

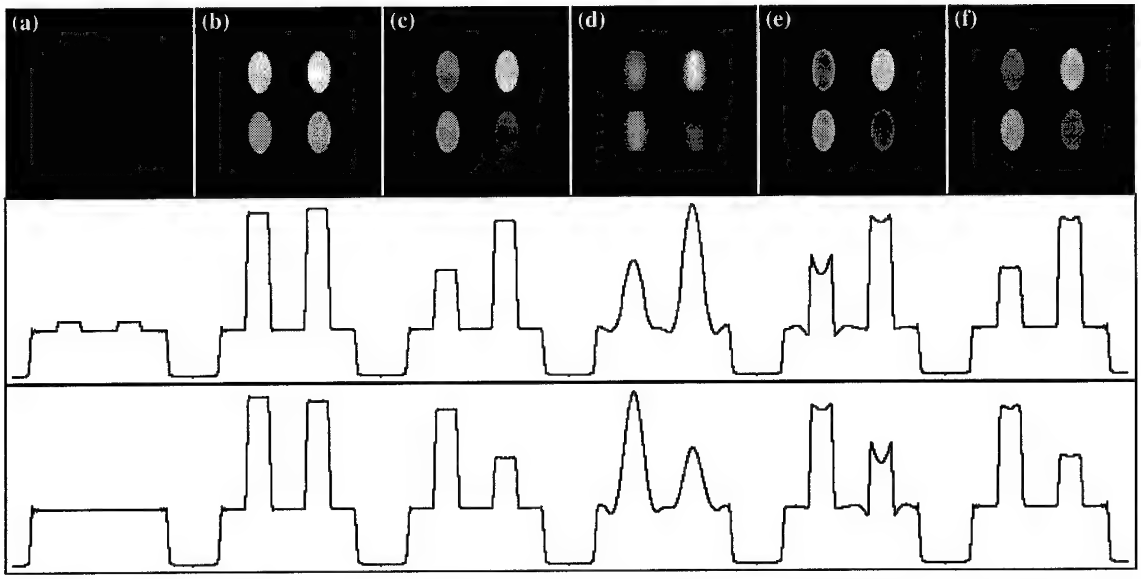

Figure 4.2: TRIGR With Complete Background Suppression: Images (row 1) and profiles through the upper and lower set of lesions (rows 2-3, respectively). (a)-(c) The baseline reference, active reference and dynamic images, respectively, reconstructed using 128 phase encodings. (d)-(e) The dynamic image reconstructed using 16 dynamic encodings with RIGR using the baseline and active reference images, respectively. (f) The dynamic image reconstructed using 16 dynamic encodings with TRIGR.

reconstructed using 128 phase encodings. Images (c)-(f) were reconstructed with 16 dynamic encodings using RIGR with the precontrast reference, RIGR with the postcontrast reference and the proposed method, respectively. The improvement from using TRIGR is much less in this case than in Fig. 4.2, because the background is not as well suppressed.

The results of all constrained image reconstruction techniques depend upon the validity of the *a priori* constraints. As with RIGR, the results of the proposed method depend upon the choice of the baseline reference image. In addition, the active reference image will also affect the outcome of the TRIGR reconstruction process. As would be expected, the more similar the baseline or active reference image is to the dynamic image, the better the reconstruction. This effect is illustrated in the following simulation, which investigates the performance of the TRIGR algorithm

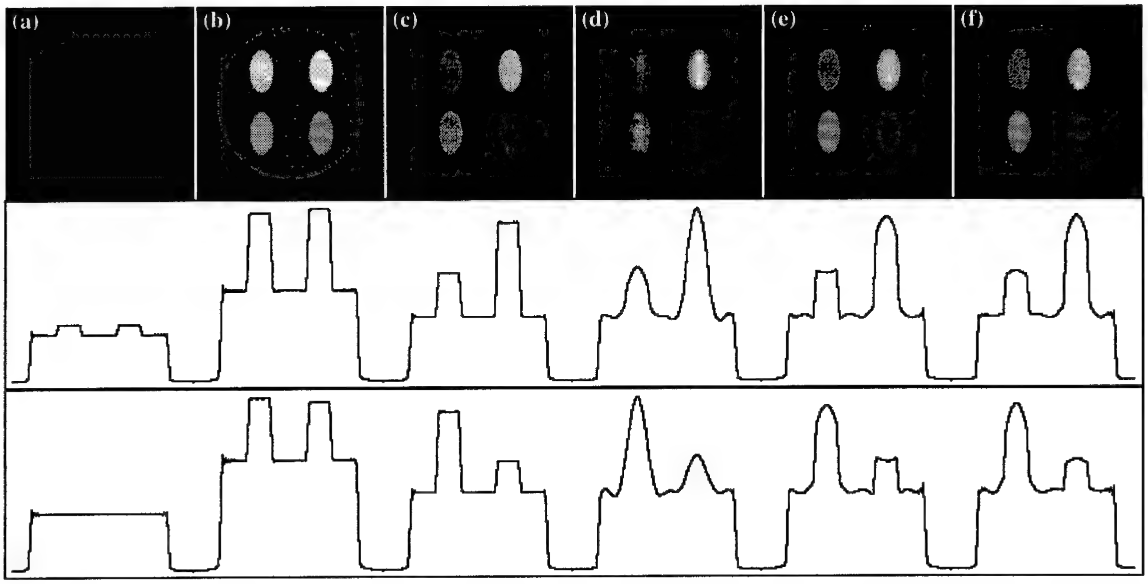

Figure 4.3: TRIGR With Incomplete Background Suppression: Images (row 1) and profiles through the upper and lower set of lesions (rows 2-3, respectively). (a)-(c) The baseline reference, active reference and dynamic images, respectively, reconstructed using 128 phase encodings. (d)-(e) The dynamic image reconstructed using 16 dynamic encodings with RIGR using the baseline and active reference images, respectively. (f) The dynamic image reconstructed using 16 dynamic encodings with TRIGR.

with different active reference images. The reference images shown in the top row of Fig. 4.4 are from different time points in a contrast-enhanced dynamic imaging simulation. Rows 2 and 3 show profiles through the upper and lower set of lesions, respectively. All of the images in this figure were reconstructed using 128 phase encodings.

Figure 4.5 rows 1-3 show the resulting images and profiles through the upper and lower set of lesions, respectively, of a TRIGR simulation in which Fig. 4.4(d) was used as the dynamic image. For comparison purposes, Fig. 4.5(a) is the dynamic image reconstructed using 128 phase encodings. Figures 4.5(b)-(f) show the TRIGR reconstruction obtained with eight dynamic encodings using Fig. 4.4(a) as the baseline reference image and Figs. 4.4(b)-(f), respectively, as the active reference image. Therefore, (b)-(c) use an active reference that is less enhanced than the dynamic

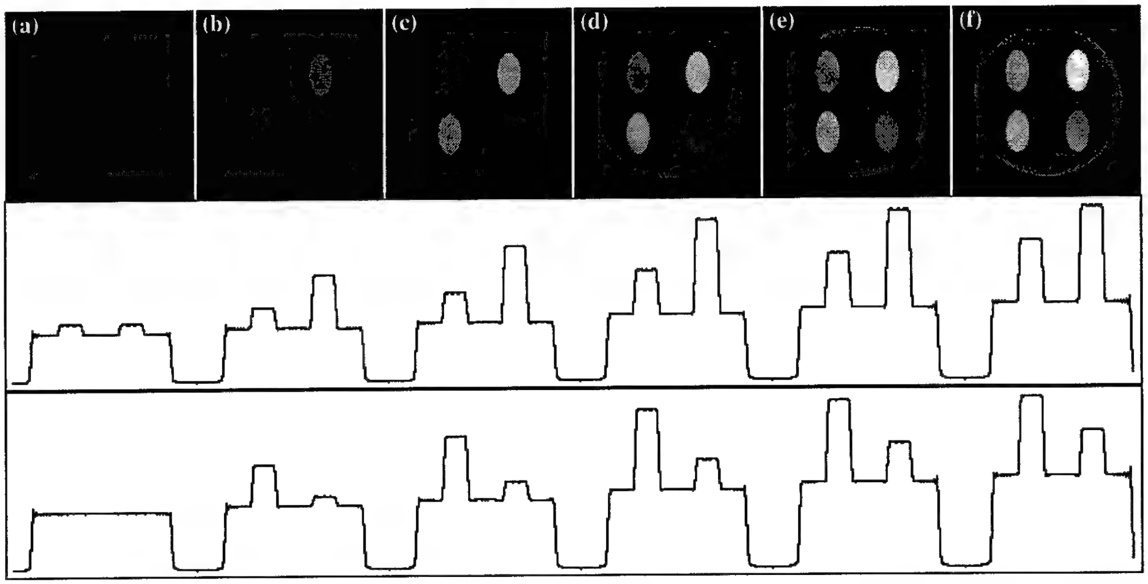

Figure 4.4: Contrast-enhanced Simulation Reference Images: Row 1 shows images from different time points in a contrast-enhanced dynamic imaging simulation reconstructed using 128 phase encodings. Rows 2 and 3 show profiles through the upper and lower set of lesions, respectively.

image, (e)-(f) use an active reference that is more enhanced than the dynamic image, and (d) uses the ideal active reference image, i.e., the dynamic image itself. Note that the lesion reconstruction is improved with a more similar reference image. This suggests that, in some situations, it may be desirable to acquire reference images at various points in the experimental procedure and then use the appropriate two references for the reconstruction of a particular dynamic image.

The effect of the choice of active reference image can be seen in actual MRI images such as those shown in Fig. 4.6. The data for this simulation is from a contrast-enhanced dynamic imaging study of a rat with breast cancer. A spin-echo sequence (TR 300/TE 20) was used to collect the data. A high-resolution precontrast reference data set was first acquired. The contrast agent was then injected and a series of dynamic data sets was acquired as the contrast agent washed into the slice. One of the data sets from the dynamic imaging period was selected as the dynamic data set for this simulation. Two of the other data sets were used for the active reference images.

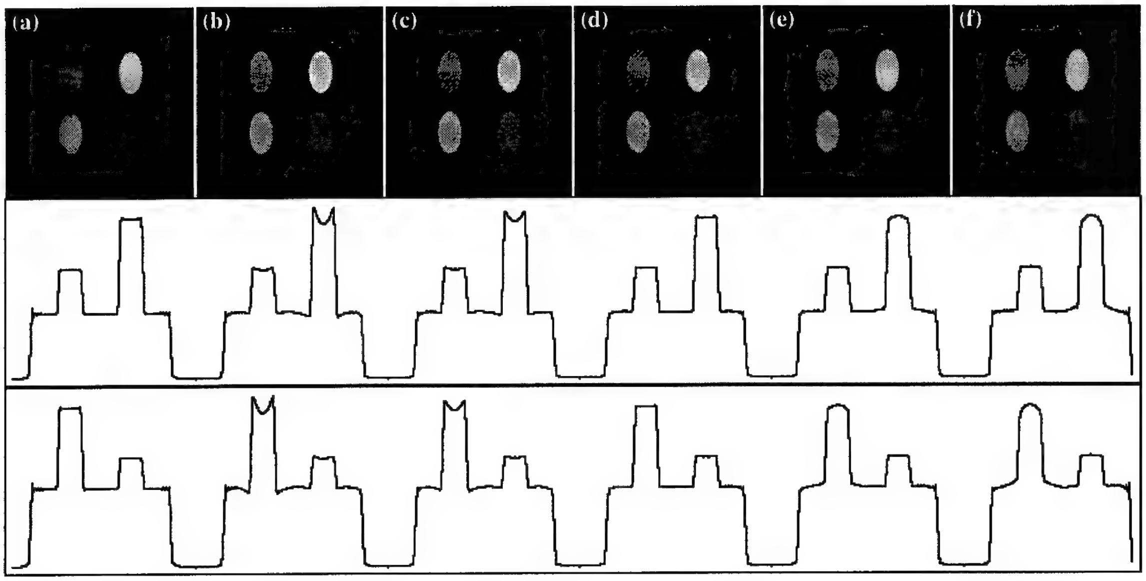

Figure 4.5: TRIGR with Different Active Reference Images: Images (row 1) and profiles through the upper and lower set of lesions (rows 2-3, respectively). (a) Dynamic image reconstructed using 128 phase encodings. The remaining images (b)-(f) were reconstructed with TRIGR using Fig. 4.4(a) as the baseline reference, Fig. 4.4(d) as the dynamic image and Fig. 4.4(b)-(f), respectively, as the active reference. The TRIGR images were reconstructed using eight dynamic phase encodings.

Figures 4.6 (a)-(d) are the precontrast reference image, a less-enhanced postcontrast reference image, a more-enhanced postcontrast reference image, and the dynamic image, respectively, reconstructed using 256 phase encodings. Figures 4.6(e)-(f) show the TRIGR reconstruction resulting from using eight dynamic encodings with (b) and (c), respectively, as the postcontrast reference image. The influence of the active reference image can easily be seen in (e)-(f). Because only eight dynamic encodings were used, the effect of the active reference image on the reconstructed dynamic image is stronger than if a larger number of dynamic encodings were used.

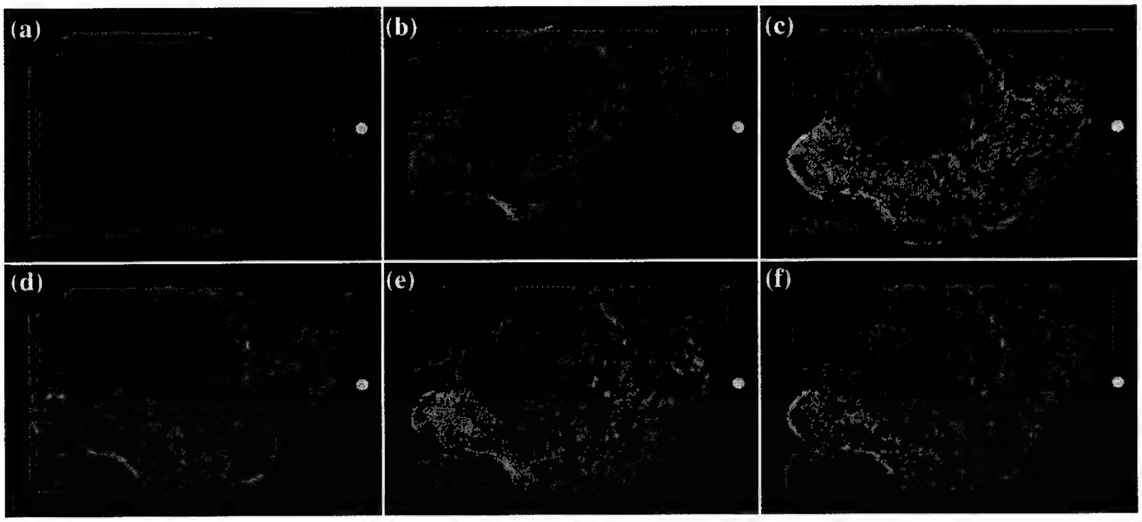

Figure 4.6: Contrast-enhanced Study Images: (a)-(c) are the precontrast reference image and two different postcontrast reference images reconstructed using 256 phase encodings. (d) The dynamic image reconstructed using 256 phase encodings. (e)-(f) The dynamic image reconstructed using TRIGR with eight dynamic encodings using (b)-(c), respectively, as the postcontrast reference image. This corresponds to a less-enhanced postcontrast reference image for (e) and a more-enhanced postcontrast reference image for (f).

4.3 Summary

The proposed dynamic imaging method can produce improved dynamic images over the original RIGR method, if the difference reference image can provide a level of suppression of the background information. The benefit derived from the proposed method increases with the level of background suppression. The method should prove valuable in applications such as contrast-enhanced dynamic studies, functional imaging, and interventional MRI.

CHAPTER 5

GS WITH EXPLICIT BOUNDARY CONSTRAINTS

Recall that the GS reconstruction formula is given by

$$\hat{I}_{\text{dyn}}(r) = \sum_{n} c_n \, C(r) e^{-i2\pi n \Delta k r}. \tag{5.1}$$

Clearly, the resulting image quality will improve as the basis functions approach those that would be derived from the dynamic image itself, i.e., if

$$C(r) e^{-i2\pi n \Delta k r} \Longrightarrow I_{\text{dyn}}(r) e^{-i2\pi n \Delta k r}. \tag{5.2}$$

In particular, because the GS coefficients c_n are global, the better the contrast relationship in the constraint function $C(r)$ matches that in the dynamic image, the better the resulting reconstruction. If the contrast in the reference and dynamic images is the same, it is helpful to build the reference contrast information into the GS basis functions. On the other hand, if the contrast relationship is not the same, only the boundary information from the reference image should be used to constrain the reconstruction. The proposed method uses explicit edge information from the reference image along with contrast information from the dynamic data to improve the GS basis functions. This differs from the GS methods described earlier, which use the dynamic data only to determine the GS coefficients.

The proposed method is particularly applicable for dynamic imaging applications such as contrast-enhanced studies in which the contrast relationship between regions of the image can differ significantly from that seen in a precontrast or postcontrast reference image. By modifying the contrast in the reference image to more closely align with that of the dynamic image, the GS basis functions derived from the new

reference image will be better able to represent the dynamic image, leading to an improved dynamic image reconstruction.

5.1 Generalized Series Model With Explicit Edge Constraints

The GS model represents the dynamic image as a contrast modulation of the underlying high-resolution reference image as

$$I_{\mathrm{dyn}}(r) = I_{\mathrm{ref}}(r) \sum_{n \in \mathcal{N}_{\mathrm{dyn}}} c(n) e^{-i 2\pi n \Delta k r} = I_{\mathrm{ref}}(r)\, C_m(r), \tag{5.3}$$

where $C_m(r)$ is the contrast modulation function. Therefore, the dynamic changes reproduced by the GS model may not have the same resolution as the reference image, because the contrast modulation function is limited by the number of terms in the model, which is in turn determined by the number of dynamic encodings. To alleviate this problem, the proposed method seeks to incorporate dynamic information into the basis functions in addition to the GS parameters.

To illustrate this idea, consider segmenting the reference image and selecting $N_{reg} < N$ of the most important regions $\mathcal{R}_n$, where N is the number of dynamic encodings. To a first approximation, the difference between the dynamic and reference images can be represented as

$$I_{\mathrm{diff}}(r) = \begin{cases} d_n & r \in \mathcal{R}_n \\ 0 & \text{else.} \end{cases} \tag{5.4}$$

In the 1D case, this can also be expressed as

$$I_{\mathrm{diff}}(r) = \sum_{n=1}^{N_{reg}} d_n \left[U(r - e_n) - U(r - e_{n+1})\right], \tag{5.5}$$

where U is the unit step function and e_n are the edges extracted from the high-resolution reference image. The d_n can be obtained by fitting the difference between the dynamic data and the corresponding encodings of the reference data to the model in Eq. (5.5). The resulting dynamic change image will have high-resolution dynamic

variations, because the region boundary locations are not limited by the number of dynamic encodings. To utilize this information in the GS model, a new reference image is created as

$$\hat{I}_{\text{ref}}(r) = I_{\text{ref}}(r) + I_{\text{diff}}(r). \tag{5.6}$$

The resulting GS basis functions will contain dynamic information.

Higher-order dynamic changes can be modeled through the use of a higher-order polynomial model or another set of basis functions, such as wavelets, in each region. However, this leads to problems for this application due to the large amount of data that would be required for reliable fitting. For the example above of modeling each region with a boxcar function, if the edges are known exactly, one parameter per region is necessary to characterize the function exactly. Higher-order behavior would require a corresponding increase in the number of parameters. Due to the small amount of dynamic data that is available in this application, the number of regions and the model order in each region must be limited to ensure the stability of the fitting step. This leads to an averaging of adjacent regions, resulting in a blurring effect.

To alleviate this problem, the proposed method determines the average signal magnitude change for each of the regions detected by the edge extraction. Therefore, because no fitting step is required, all of the regions can be used, which reduces the averaging effect. As mentioned earlier, the extracted edges are used to determine the dynamic change between the reference image and dynamic image, as opposed to the new reference image itself. This will further reduce the averaging effect, as well as reduce the adverse effects of edges that are not accurately detected by the edge extraction step.

For this application, a multiscale edge detection approach is desirable, because it is expected that image edges will appear at many scales. In addition, the boundary extraction step should result in closed edges to allow easy determination of the regions in the image. The particular method used for this research was the multiresolution edge detection scheme developed by Ahuja [89,90]. In contrast to the multiscale edge

detection that can be performed by some wavelet transforms, the concept of scale in the multiresolution edge detection scheme relates to both physical proximity and greyscale similarity, as opposed to the size of the edge itself, which is beneficial for this application.

The specific steps for applying the proposed method to a high-resolution reference image and a low-resolution dynamic data set are as follows. First, a zero-padded difference image I_{diff} is created by subtracting the corresponding reference encodings from the dynamic encodings and reconstructing using the zero-padded Fourier tranform. For each of the regions detected in the reference image, the average magnitude of the zero-padded difference image is calculated. (Note that the number of regions used is not limited by the number of dynamic encodings.) The result will be an image of the average signal magnitude change in each of the regions. The phase of the zero-padded difference image is reintroduced during the creation of the new constraint function for the GS model. If the original constraint function is a baseline reference image, the new reference image is

$$\hat{I}_{\text{baseline}} = I_{\text{baseline}} + I_{\text{diff,ave}}\, e^{i\angle I_{\text{diff}}}, \tag{5.7}$$

or, for the active reference case, the new reference image is

$$\hat{I}_{\text{active}} = I_{\text{active}} - I_{\text{diff,ave}}\, e^{i\angle I_{\text{diff}}}, \tag{5.8}$$

where $I_{\text{diff,ave}}$ is the average signal magnitude change image and $\angle I_{\text{diff}}$ is the phase of the zero-padded difference image. This new reference image is used as the constraint function in the GS model to reconstruct the dynamic image.

5.2 Results and Discussion

The proposed method was compared to the original RIGR method with computer simulations on experimental MRI data using both baseline and active reference images. The experimental data shown here are from the contrast-enhanced dynamic imaging study of a cancerous rat described in Chapter 4. As before, the central N encodings of the dynamic data sets were used as the reduced-encoding dynamic data.

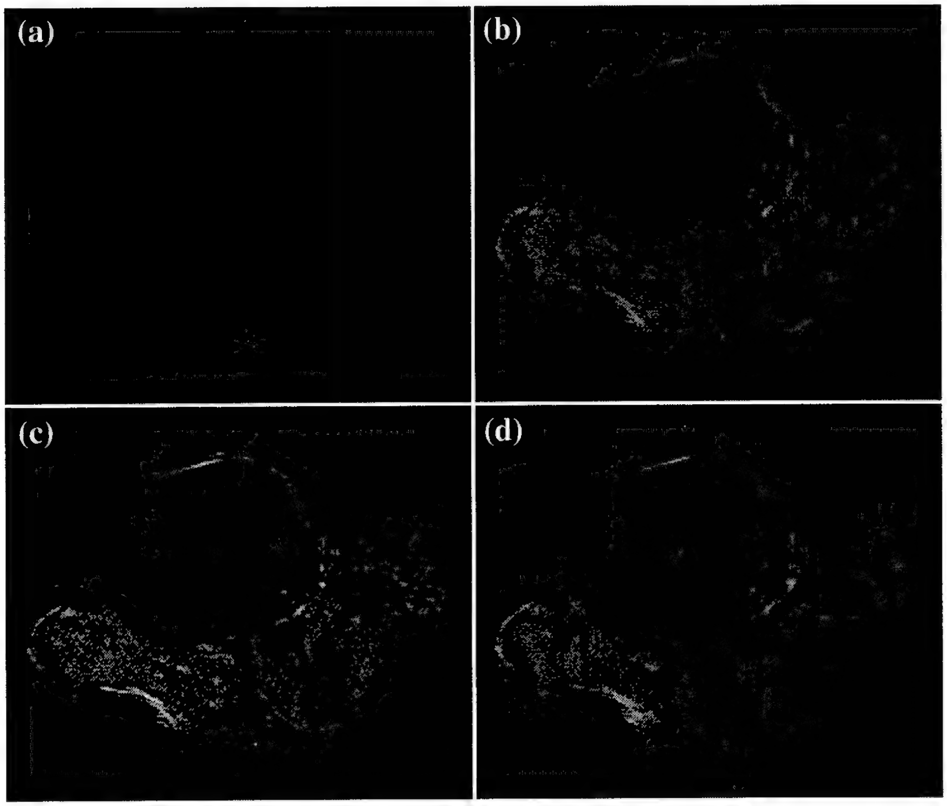

Figure 5.1: Explicit Edge Information with Precontrast Reference Image: (a)-(b) The original precontrast reference and dynamic images, respectively, reconstructed using 256 phase encodings. (c)-(d) The dynamic image reconstructed using 32 dynamic encodings with the original RIGR method and the proposed method, respectively.

The results of applying the proposed method with a precontrast reference image are shown in Fig. 5.1. Images (a)-(b) are the original reference and dynamic images, respectively, reconstructed using 256 phase encodings. Images (c)-(d) are the dynamic image reconstructed using 32 dynamic encodings with the original RIGR method and the proposed method, respectively. Note the improved reproduction of the signal magnitude in the contrast-enhanced tumor with the proposed method.

The edge extraction step appears to currently be the limiting step in the process. In the RIGR image of Fig. 5.1(d), the blockiness of the detected regions is apparent, in particular at the outer edges of the lesion. This can be reduced in some situations

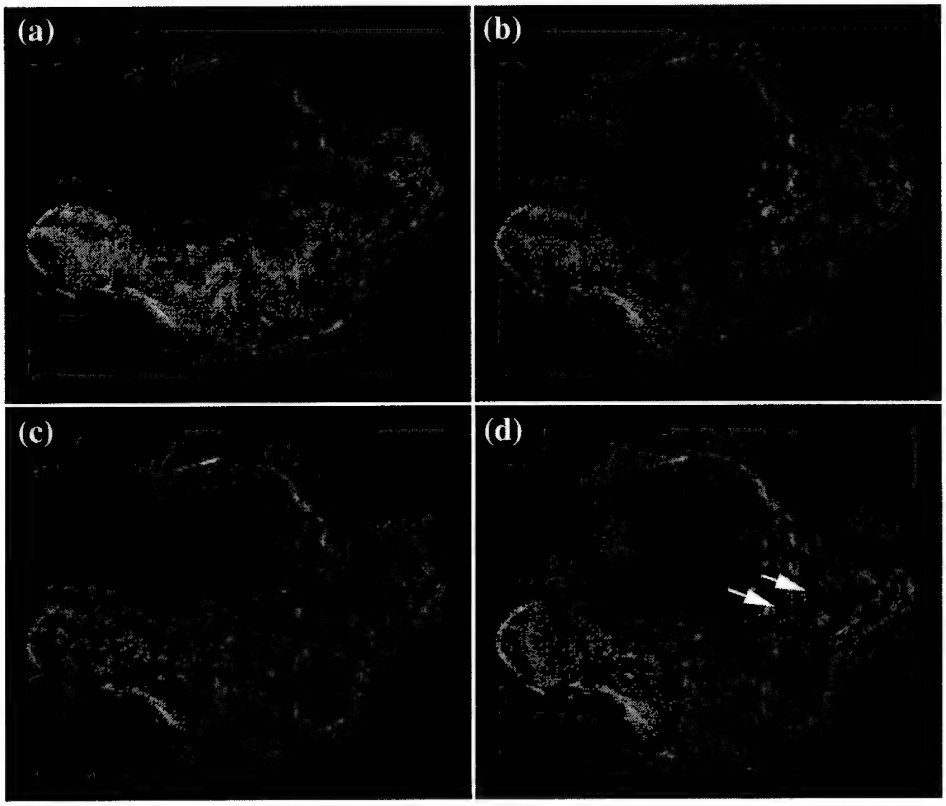

Figure 5.2: Explicit Edge Information with Postcontrast Image: (a)-(b) The original postcontrast reference and dynamic images, respectively, reconstructed using 256 phase encodings. (c)-(d) The dynamic image reconstructed with 32 dynamic encodings using the original RIGR method and the proposed method, respectively.

by using an active reference image in which the contrast between adjacent regions is larger, making it easier for the edge extraction step to detect the edges well. In addition, if there is no edge information about a new feature in the reference image, the edge extraction step will not capture it. The result is that the new feature will be averaged in with a surrounding area in the contrast difference determination step. This also supports the use of an active reference image, because it may contain additional edges introduced by the dynamic changes.

Both of these effects can be seen in Fig. 5.2, which shows the results of using edge information extracted from a postcontrast reference image. Images (a)-(b) are

the original postcontrast reference image and the dynamic image, respectively, reconstructed using 256 phase encodings. Images (c)-(d) show the dynamic image reconstructed with 32 dynamic encodings using the original RIGR method and the proposed method, respectively. Image (d) has a sharper reproduction of some of the internal details of the tumor such as those indicated by the arrows. However, the improvement between (c)-(d) is not as great as between Figs. 5.1(c)-(d) because the contrast in the postcontrast reference image is more similar to the dynamic image than the contrast in the precontrast reference image.

5.3 Summary

A method has been developed to use explicit edge information extracted from a high-resolution reference image to inject dynamic information into the GS basis functions. If possible, it is preferable to use an active reference image for the edge extraction step, because it may result in better detection of the image regions.

CHAPTER 6

MOTION-COMPENSATED DYNAMIC IMAGING

Object motion is often a problem for MR imaging. For convenience, it is useful to categorize object motion in terms of its temporal and physical characteristics. If the motion occurs during one T_R period, it is referred to as intraview motion; whereas, motion that occurs between T_R periods is called interview motion. In addition, motion that occurs between complete data sets is called interset motion. In conventional MRI, intraview and interview motion of the object can cause image artifacts, because it destroys the encoding relationship in the imaging equation, although the former is not usually a problem due to the short times involved. In addition to intraview and interview motion, interset motion is also a problem for constrained dynamic imaging, because motion of the object between the reference and dynamic data sets can render the reference information useless as a constraint for image reconstruction.

An approach to overcome this problem is to detect the object motion before the constrained reconstruction step is performed. However, detection of object motion in reduced-encoding dynamic imaging is nontrivial due to several factors. First, dynamic image contrast changes and object motion are mixed together. Second, the dynamic data sets are low-resolution, and it is usually necessary to detect motion to a higher accuracy than that dictated by the low-resolution Fourier pixel size. To overcome these problems, we propose to use a similarity norm which can accurately detect the motion in spite of the contrast changes and the low-resolution nature of the dynamic data. The similarity norm tries to remove the effects of the contrast change by using only the edges from the high-resolution reference image for the motion estimation.

6.1 Similarity Norm-Based Motion Estimation

Given two images I_1 and I_2, we assume that

$$I_2(x, y) \sim I_1(x \cos\theta_0 - y \sin\theta_0 + x_0, x \sin\theta_0 + y \cos\theta_0 + y_0). \tag{6.1}$$

That is to say, there is a relative rigid-body rotation and translation between I_1 and I_2, as specified by x_0, y_0, and θ_0. The tilde signifies that I_1 and I_2 can have different contrast behavior. Therefore, the goal of the motion-estimation step is to find x_0, y_0, and θ_0.

Assuming that I_2 is a low-resolution image and I_1 is a high-resolution image, we first segment I_1 into a number of "homogeneous" regions. The strategy here is to use these region boundaries as landmark features. We superimpose this region structure onto I_2 and then calculate the regional intensity inhomogeneity σ_l^2. We argue that this inhomogeneity is a good indicator of the misalignment between the two images. Specifically, we define the misalignment error E_a as

$$E_a = \sqrt{\sum_{l=1}^{N_{\text{reg}}} \frac{m_l}{N} \sigma_l^2}, \tag{6.2}$$

where N_{reg} is the number of regions, m_l is the number of pixels in each region and N is the total number of pixels. Clearly, the value of E_a is a function of the motion parameters. By minimizing E_a, the values of x_0, y_0, and θ_0 can be found. The estimated-motion parameters that minimize E_a are then used in the GS model as

$$\hat{I}_{\text{dyn}}(r) = T_{est} I_{\text{ref}}(r) \sum_{n \in \mathcal{N}_{\text{dyn}}} c_n e^{-i2\pi n \Delta k r}, \tag{6.3}$$

where T_{est} is the transformation that corresponds to the estimated-motion parameters.

The proposed method is applied to a sequence of dynamic images in turn, so that the dynamic data set is compared to a high-resolution image that should have a more similar edge structure than the original reference image. First, the motion between the high-resolution reference image and the first dynamic data set is measured. These measurements are used to correct and reconstruct the first GS dynamic image. This

high-resolution GS image is used with the second dynamic data set to determine the motion that occurred between these two acquisition times. The cumulative motion measurements are used with the reference image to reconstruct the second GS dynamic image. This procedure is repeated for the entire image sequence. Note that the dynamic image is reconstructed using the original high-resolution reference image to reduce errors that could arise due to the accumulated motion correction.

If it cannot be assumed that no appreciable motion occurs during the collection of a particular reduced-encoding dynamic data set, other methods will have to be employed to measure this intraset motion. One possible way to do that is by using navigator techniques [91] that acquire a "navigator echo" during each view in addition to the image information. Each navigator echo is then compared to an initial reference navigator echo using correlation [91] or a least squares technique [92–94] to determine the motion along the navigator direction. Additional navigator echoes can be used to measure motion in the other directions, or orbital navigator echoes [93] can be used to simultaneously measure the two directions of translation and rotation in a plane. Although the navigator techniques are being used in many applications, the methods cannot be directly applied to dynamic imaging, because the basic assumption of the navigator echo method will be violated; namely, that all of the changes in the navigator data are due to motion of the object. This causes a problem in dynamic imaging in which the navigator data from each view can look very different even without motion, leading to incorrect motion estimates.

One may try to get around this by comparing a navigator to the immediately preceeding navigator to determine the motion parameters as opposed to an initial reference navigator. Although this should reduce the effect of the dynamic changes on the navigator data, the incremental motion may be too small to be detected with this method. Then, because the motion at a point in time would be the accumulation of the measured incremental motions up to that time, the error in the motion estimate may become quite large.

Perhaps a better way to use the navigator method with dynamic imaging applications is to design the pulse sequence such that the navigator signal is not sensitive to

the contrast changes. For example, consider a contrast-enhanced dynamic study using a T_2 contrast agent. The T_2 contrast agent modifies the appearance of the tissues which take it up by changing the T_2 relaxation constant. Therefore, the image data should be sensitive to the change in T_2, but the effect of T_2 on the navigator data should be minimal. A possible way to accomplish this is to acquire the FID signal following the *RF* excitation pulse as the navigator data and use the echo signal as the image data. In this way, the image can be T_2 weighted, but the navigator signal will be proton density weighted. This method would require careful design of the pulse sequence with the given application in mind.

In many cases, the motion may occur in three dimensions, as opposed to the planar motion discussed here. In this case, the solution will depend upon whether the imaging sequence is acquiring 2D slices or a 3D volume. In the case of 2D slices, the excitation and signal reception locations will need to be dynamically adapted based on the detected motion perpendicular to the imaging plane [95]. The in-plane motion can then be addressed, as discussed previously. For 3D imaging, the motion detection scheme would have to be expanded to detect all six degrees of motion (three translations and three rotations).

6.2 Results and Discussion

Computer simulations were performed to characterize the motion artifacts that can arise with the generalized series (GS) model due to interset motion. The simulations investigated the three in-plane motions: translation in the phase-encoding direction, translation in the frequency-encoding direction, and rotation. The reference image shown in Fig. 6.1(a) was used for all cases in the simulation. The high-resolution dynamic image is shown in Fig. 6.1(b) for the case of no translation or rotation from the reference position. Both of these images were reconstructed using 128 phase-encodings.

The first motion that was investigated was translation in the phase-encoding direction. Figure 6.2 rows 1-3 show the dynamic image and profiles through the upper

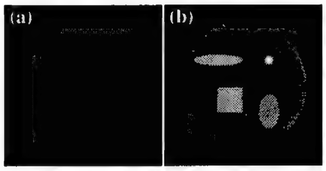

Figure 6.1: Motion Study High-Resolution Images: (a)-(b) Precontrast reference image used for all simulations and dynamic image with no translation or rotation from the reference position, respectively. Both images were reconstructed using 128 phase-encodings.

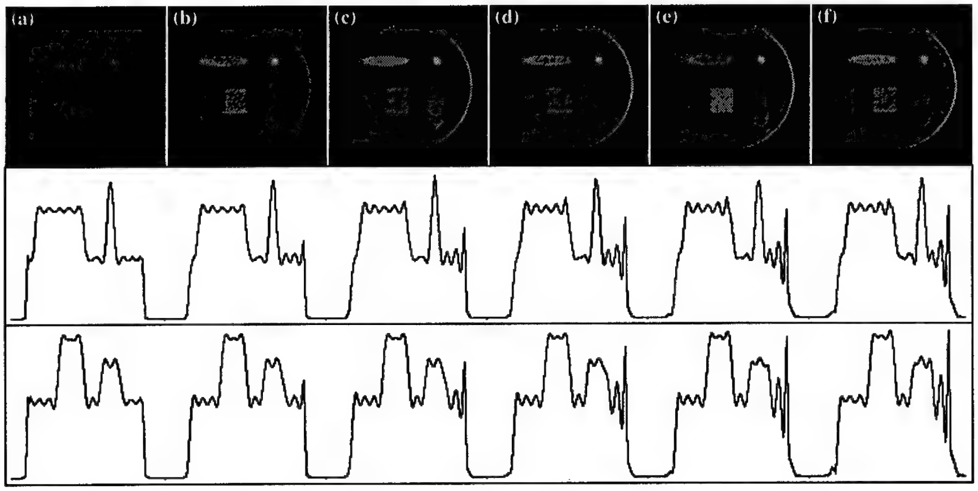

Figure 6.2: Motion Study (Translation in Phase-Encoding Direction): (rows 1-3) Dynamic images and profiles through the upper and lower lesions, respectively, reconstructed using GS with 32 dynamic encodings for translations of 0, 1, 2, 3, 4 and 5 pixels ((a)-(f), respectively) in the phase-encoding direction (horizontal) between the reference and dynamic data acquisitions.

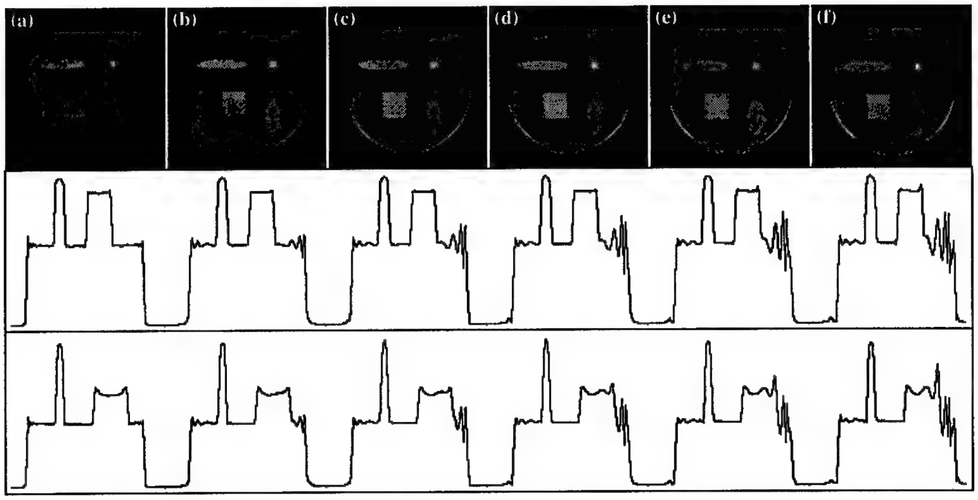

Figure 6.3: Motion Study (Translation in Frequency-Encoding Direction): (rows 1-3) Dynamic images and profiles through the left and right lesions, respectively, reconstructed using GS with 32 dynamic encodings for translations of 0, 1, 2, 3, 4 and 5 pixels ((a)-(f), respectively) in the frequency-encoding direction (vertical) between the reference and dynamic data acquisitions.

and lower set of lesions, respectively, reconstructed using 32 dynamic encodings with the GS model. Images (a)-(f) correspond to a translation of 0, 1, 2, 3, 4 and 5 pixels, respectively, in the phase-encoding direction (horizontal) between the reference and the dynamic data sets. Note the ringing artifact extending from the right side of the phantom. As would be expected, the ringing is worse for larger motions and for a smaller number of dynamic encodings. Note that these artifacts arise, even though the translation is smaller in all cases than the low-resolution Fourier pixel size.

The simulations were repeated for translation occurring in the frequency-encoding direction (vertical) between the acquisition of the reference and dynamic data sets. The dynamic image and profiles through the left and right set of lesions resulting from a GS reconstruction using 32 dynamic encodings are shown in Fig. 6.3 rows 1-3, respectively. Images (a)-(f) involve a translation of 0, 1, 2, 3, 4 or 5 pixels, respectively, in the frequency-encoding direction (vertical) between the reference and dynamic data sets. In this case, the result is also a ringing artifact emanating from one

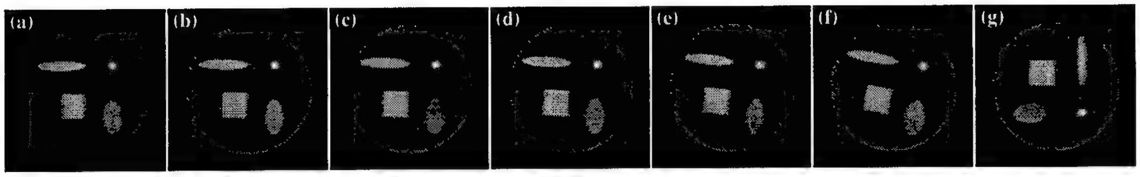

Figure 6.4: Motion Study (Rotation): (a)-(g) Dynamic image reconstructed with GS using 32 dynamic phase-encodings for rotations of 0, 1, 2, 3, 6, 10 and 90 clockwise degrees, respectively, between the reference and dynamic data acquisitions.

side. However, the nature of the ringing is slightly different from that seen with the motion in the phase-encoding direction. This is due to the fact that the GS model is applied along the (low-resolution) phase-encoding direction, and the Fourier transform is applied along the (high-resolution) frequency-encoding direction. As before, the artifacts are worse for increasing motion and a decreasing number of dynamic encodings.

The last planar motion to be investigated was rotation. Figures 6.4(a)-(g) show the dynamic image reconstructed using 32 phase-encodings with the GS model for a rotation of 0, 1, 2, 3, 6, 10 and 90 clockwise degrees, respectively, between the reference and dynamic data sets. In this simulation, a slight blurring in the phase-encoding direction of the edges of internal structures results. The blurring increases with increasing rotation and a decreasing number of dynamic encodings. Because the outer boundary of the phantom is symmetric, no effect from the rotation is seen in the reconstruction of the outer boundary.

To avoid these motion artifacts, it is necessary to detect and correct for motion that occurs between the acquisition of the reference and dynamic data sets prior to constrained reconstruction. The proposed method has performed well when applied to a sequence of dynamic images, as discussed earlier. The results of applying the proposed method to a contrast-enhanced dynamic study of a rat with cancer are shown in Fig. 6.5 in which (a) is the reference image that was reconstructed using 256 phase-encodings. Images (b)-(d) were reconstructed using the GS model with 32 dynamic encodings. In image (b), there was no motion between the reference and dynamic

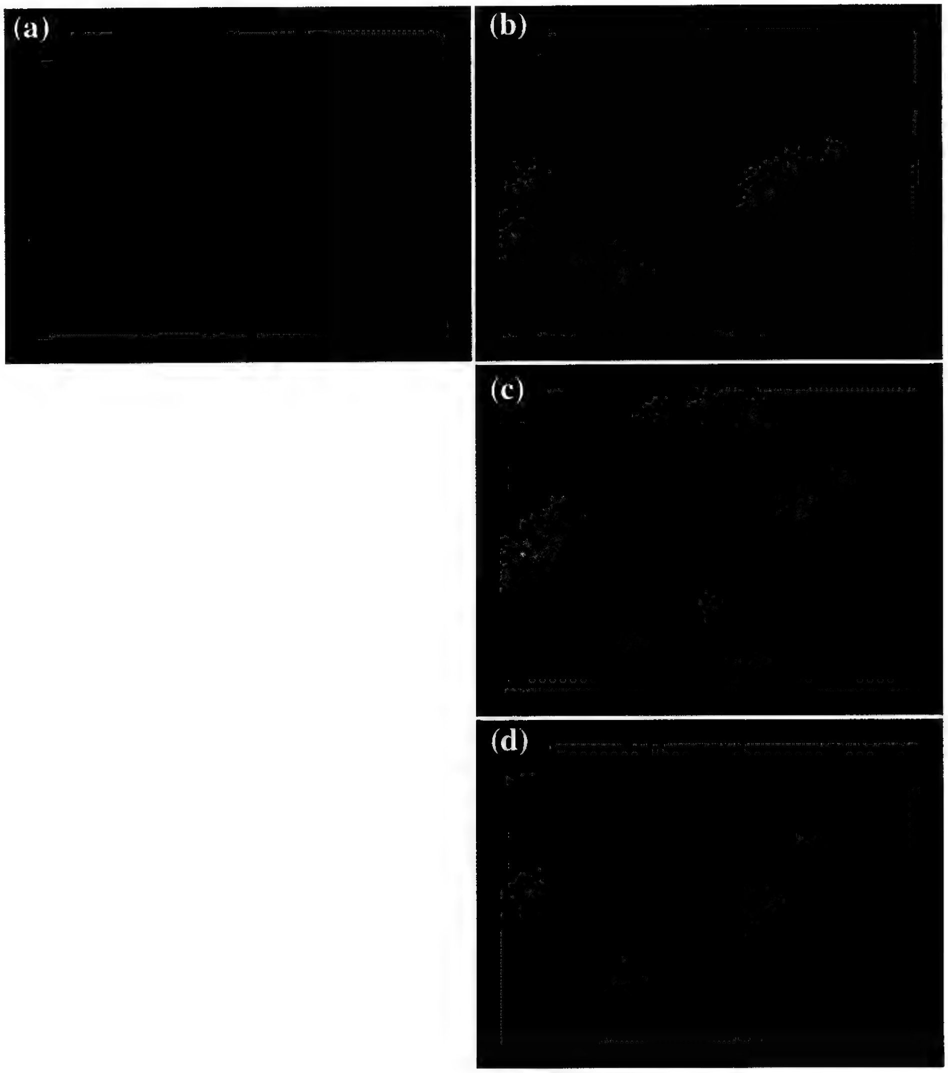

Figure 6.5: Motion Corrected Dynamic Images: (b)-(d) were reconstructed using the GS model with (a) as the reference image and 32 dynamic encodings. (b) The dynamic image that results with no motion between the reference and dynamic data sets. The remaining images show the dynamic image reconstructed with a 5 pixel shift in the phase-encoding direction (vertical), a -3 pixel shift in the frequency-encoding direction (horizontal) and a 3 degree clockwise rotation between the reference and dynamic data sets. (c)-(d) The dynamic images that result with no motion correction and with the proposed method, respectively. Note the reduced motion artifacts in (d) as compared to (c).

data sets, and therefore, it represents the ideal GS reconstruction. The remaining images represent a case in which the position of the object during the dynamic data acquisition has changed from the reference position by a rotation of 3 degrees and shifts of 5 and -3 pixels in the phase-encoding and frequency-encoding directions, respectively. Figures 6.5(c)-(d) were reconstructed with no motion correction and with the proposed method, respectively. Note the reduced-motion artifacts in the corrected image (d).

6.3 Summary

The motion artifacts that are seen with the GS model include ringing and blurring due to in-plane translation and rotation, respectively, between the reference and dynamic data sets. To avoid these artifacts, the motion between the data sets needs to be measured, which is a difficult problem for many reduced-encoding dynamic imaging applications. The proposed solution uses a similarity norm to accurately detect the motion in spite of the contrast changes and the low-resolution nature of the dynamic data.

CHAPTER 7

FUTURE WORK AND CONCLUSIONS

7.1 Future Work

- **3D RIGR/TRIGR:** For many dynamic imaging applications, it would be desirable to do full 3D imaging, as opposed to a stack of 2D slices. An example is contrast-enhanced breast imaging, in which high-spatial resolution in 3 dimensions would reduce the risk of a missed lesion. This would require that the RIGR/TRIGR algorithms be extended to 3D. In order to do this, it is necessary to solve a block-Toeplitz system to determine the GS coefficients. If it was desired to use explicit edge information or motion compensation, the edge extraction technique and motion measurement method would both need to be extended to 3D. It may be necessary to investigate faster algorithms to perform all of these functions for the 3D case due to the vast amount of data involved.

- **Locally Focused RIGR/TRIGR:** Given the *a priori* knowledge that the dynamic changes will occur in a certain region of the image, it may be possible incorporate this information with the GS model to obtain a better reconstruction in that area of the dynamic image. This would have application in, for example, following the progress of a needle biopsy in interventional MRI. This work may involve the development of better methods of background suppression to allow the GS basis functions to only represent the dynamic changes in the region of interest.

- **Contrast-Immune Navigator Echoes:** As discussed in Chapter 6, it may be possible to design pulse sequences for contrast-enhanced dynamic imaging

sequences such that the navigator signal is not affected by the changing contrast due to, for example, an injected contrast agent.

- **Adaptive Data Acquisition:** If the *a priori* information that is available is a reference image, the use of this information to guide the data acquisition can result in serious image artifacts. However, it may be possible to use other types of *a priori* information to guide the data acquisition in a beneficial way.

7.2 Conclusions

The reduced-encoding dynamic MR imaging problem has been addressed with the objective of obtaining simultaneously high temporal and spatial resolutions. To avoid the loss of spatial resolution that occurs with reduced-encoding Fourier imaging, many methods make use of *a priori* information at some point in the process to reduce the number of encodings that are necessary for the dynamic images. This study reveals that if the available *a priori* information is a reference image, direct use of this information to "optimize" data acquisition using the existing wavelet transform or singular value decomposition schemes can undermine the capability to detect new image features. However, proper incorporation of the *a priori* information in the image reconstruction step can significantly reduce the resolution loss associated with reduced-encoding. For Fourier-encoded data, we have shown that the generalized-series (GS) model is an effective mathematical framework for carrying out the constrained reconstruction step.

To further improve the reconstructed image, several techniques were developed to improve the GS basis functions. The two-reference reduced-encoding imaging by generalized-series reconstruction (TRIGR) method uses a second high-resolution reference image to suppress the background information. This allows the GS basis functions to more accurately represent the areas of dynamic change. A second technique uses explicit edge information from the reference image to inject information from the dynamic data into the GS basis functions. The resulting GS basis functions more closely resemble those that would be derived from the dynamic image itself.

Finally, motion that occurs between the acquisition of the reference data set and the dynamic data set can render the reference information useless as a constraint for image reconstruction. This is a difficult problem to address, because the dynamic changes may alter the appearance of the image significantly, posing problems for both navigator-based techniques and registration algorithms. A motion compensation method is proposed which uses a similarity norm to accurately detect the motion, in spite of the contrast changes and low-resolution nature of the dynamic data. The technique was shown to significantly reduce motion artifacts in GS images.

APPENDIX A

SIGNAL-TO-NOISE RATIO

If the MRI measurement noise is assumed to be additive noise from an ergodic, stationary, white noise process with zero mean and standard deviation σ_d, the resulting data can be expressed as

$$\hat{d}(k) = d(k) + \eta_d(k), \tag{A.1}$$

where $\hat{d}(k)$ is the measured noisy data, $d(k)$ is the noiseless data and $\eta_d(k)$ is the measurement noise. This noise will be transformed to the image domain during image reconstruction, resulting in the noisy image

$$\hat{I}(r) = I(r) + \eta_I(r). \tag{A.2}$$

Clearly, the resulting noise image $\eta_I(r)$ will depend upon the image reconstruction scheme used, as well as the number of encodings.

With this in mind, the signal-to-noise ratio (SNR) behavior of the Fourier series and generalized-series (GS) methods was investigated using 1D profiles. Both noiseless and noisy reconstructions of the dynamic image were created for various noise levels and various numbers of dynamic encodings. The SNR of the reference and dynamic data was the same, reflecting the common experimental implementation of the method. (If signal averaging was used to improve the SNR of the reference data, this would also affect the SNR of the resulting GS dynamic images.) The results obtained for the reduced-encoding Fourier series and generalized-series reconstructions were compared with that of the high-resolution dynamic image.

Two measures of SNR were calculated. The first measure included both random noise and systematic artifacts, and the second measure included only the random

noise component. In the first case, the noiseless dynamic image (gold standard) was subtracted from, for example, the noisy GS image, yielding a profile that included both noise and systematic artifacts. In the second case, the noiseless GS image was subtracted from the noisy GS image, leaving a pure noise profile. For each data point, the average standard deviation (SD) of the resulting profile for 1000 trials with different noise realizations was calculated to quantify the performance.

Figure A.1 shows one realization of the 1000 trials conducted with 32 dynamic encodings. Rows 1 and 2 show the noiseless and noisy, respectively, reconstructions of the reference ((a),(e)) and dynamic ((b),(f)) profiles reconstructed using 512 encodings and the Fourier series ((c),(g)) and GS ((d),(h)) profiles reconstructed using 32 dynamic encodings. Row 3 shows the difference between the noisy reconstructions (f)-(h) and the noiseless dynamic image (b). As discussed before, this gives a measure of the noise and systematic artifacts that are present in the noisy reconstructions. Row 4 shows the difference between the noisy reconstructions (f)-(h) and the corresponding noiseless reconstructions (b)-(d). Comparison of rows 3 and 4 shows that significant systematic artifacts are present in the Fourier series and GS profiles reconstructed with 32 dynamic encodings in this simulation. Note the reduced noise level in the truncated Fourier reconstruction (m) due to the reduced number of data points that are used in the reconstruction.

Figure A.2 shows the mean SD of the noise alone for the Fourier series and GS reconstructions as the number of dynamic encodings ranges from 8 to 256 of 512 encodings. As expected, the Fourier series reconstructions have a lower mean SD at every number of dynamic encodings than the high-resolution dynamic reconstruction due to the reduced number of data points used. The mean SD for the GS model is consistently higher than that of the high-resolution dynamic reconstruction. For this simulation, the mean SD of the GS reconstruction improves only slightly as a greater number of dynamic encodings is used past 32 encodings.

Figure A.3 depicts the behavior of the mean SD of the noise and systematic artifacts for the Fourier series and GS reconstructions with a varying number of dynamic encodings ranging from 8 to 256 of 512 encodings. The mean SD for the

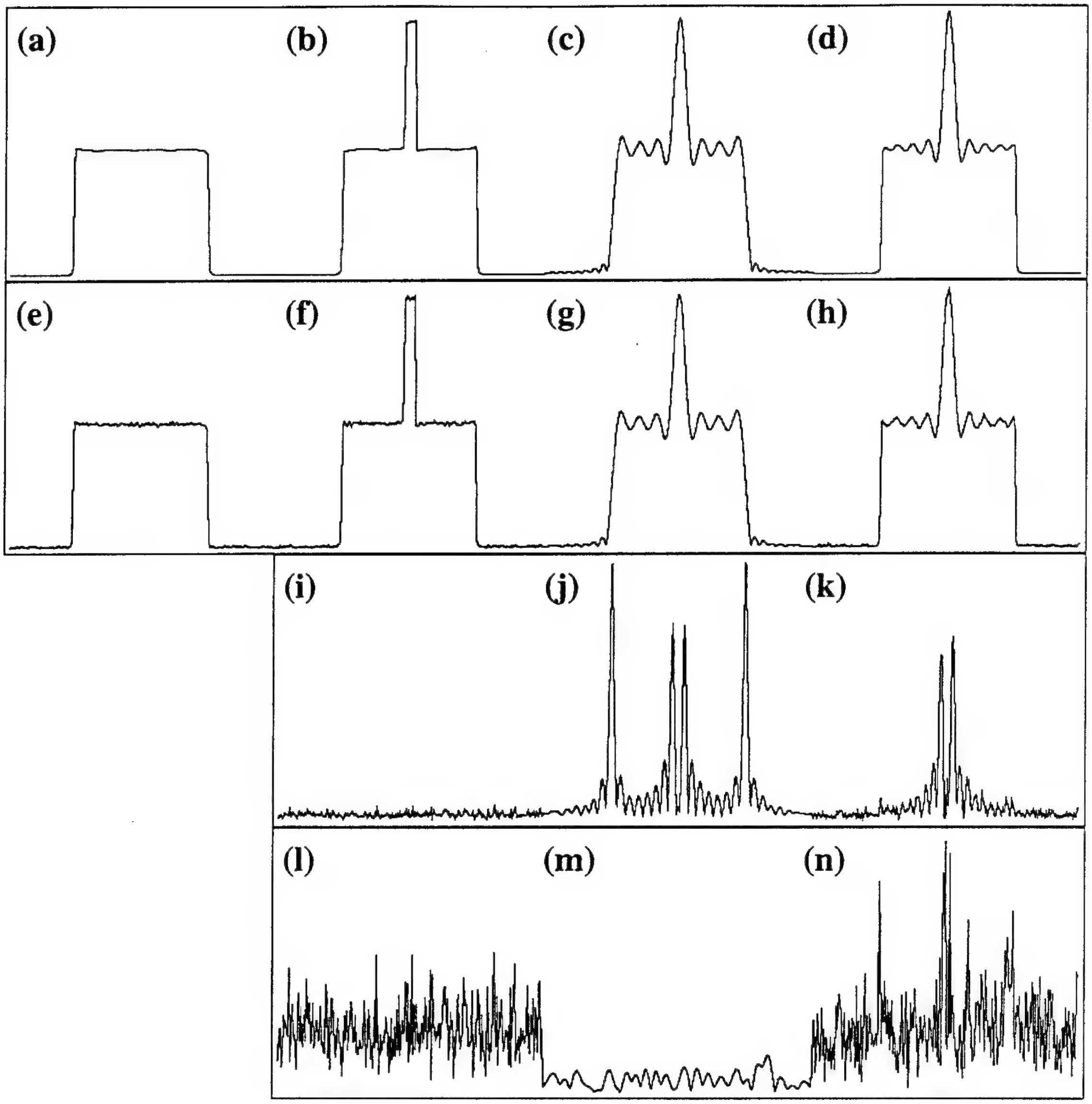

Figure A.1: SNR Study: Rows 1 and 2 are the noiseless and noisy reconstructions, respectively, of the reference ((a),(e)) and dynamic ((b),(f)) profiles reconstructed with 512 encodings and the truncated Fourier ((c),(g)) and GS ((d),(h)) profiles reconstructed using 32 dynamic encodings. Row 3 shows the difference between the noisy reconstructions (f)-(h) and the noiseless dynamic profile (b). This gives a measure of the noise and systematic artifacts that are in the noisy reconstructions. Row 4 shows the difference between the noisy reconstructions (f)-(h) and the corresponding noiseless reconstructions (b)-(d). This gives a measure of the noise performance. Note that the four rows are not on the same scale.

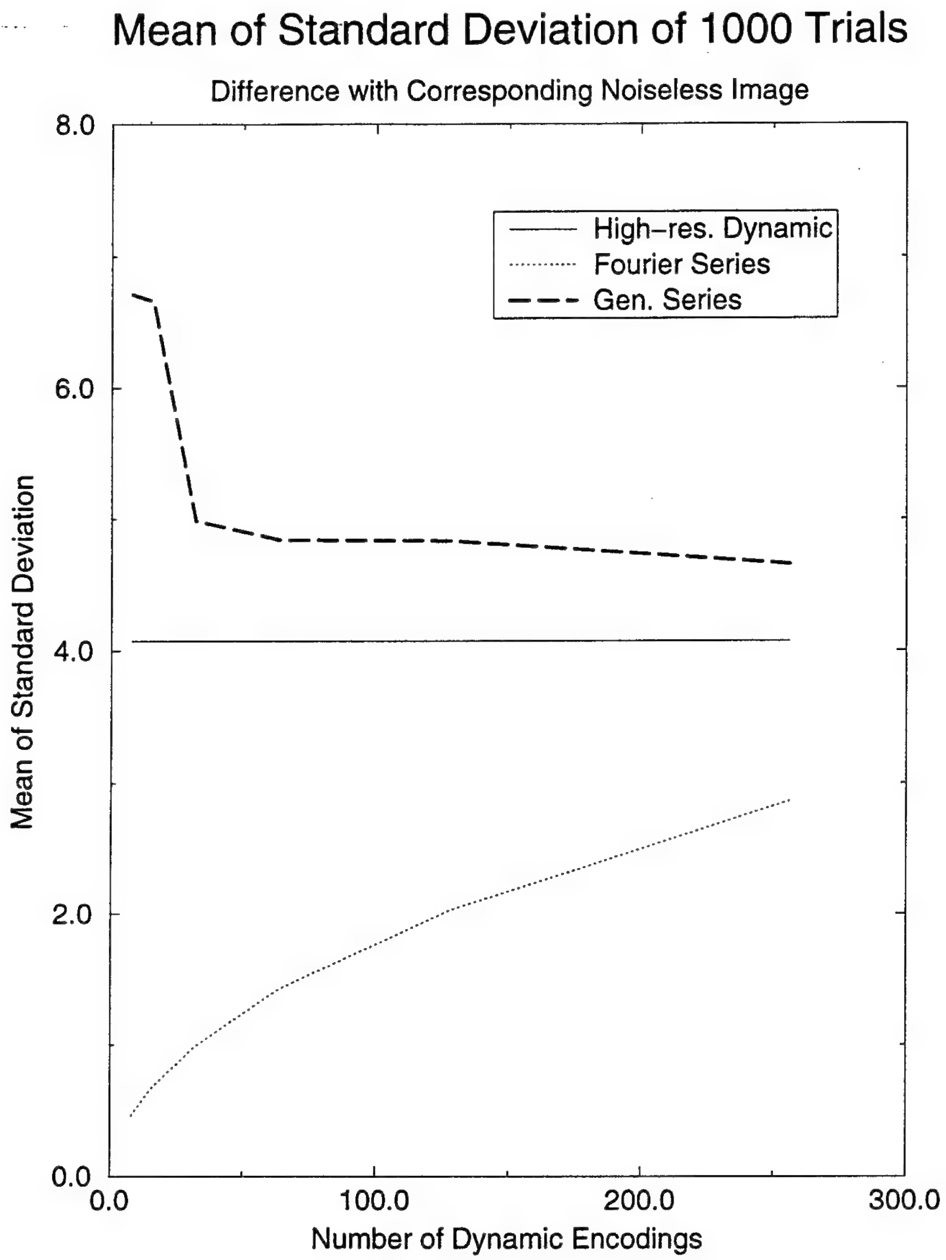

Figure A.2: SNR Behavior of Noise: Curves show the dependence of the mean SD of the noise, with respect to the number of dynamic encodings used in the reconstruction for the Fourier series and generalized-series. The mean SD from the high-resolution dynamic image is included as a horizontal line for comparison purposes.

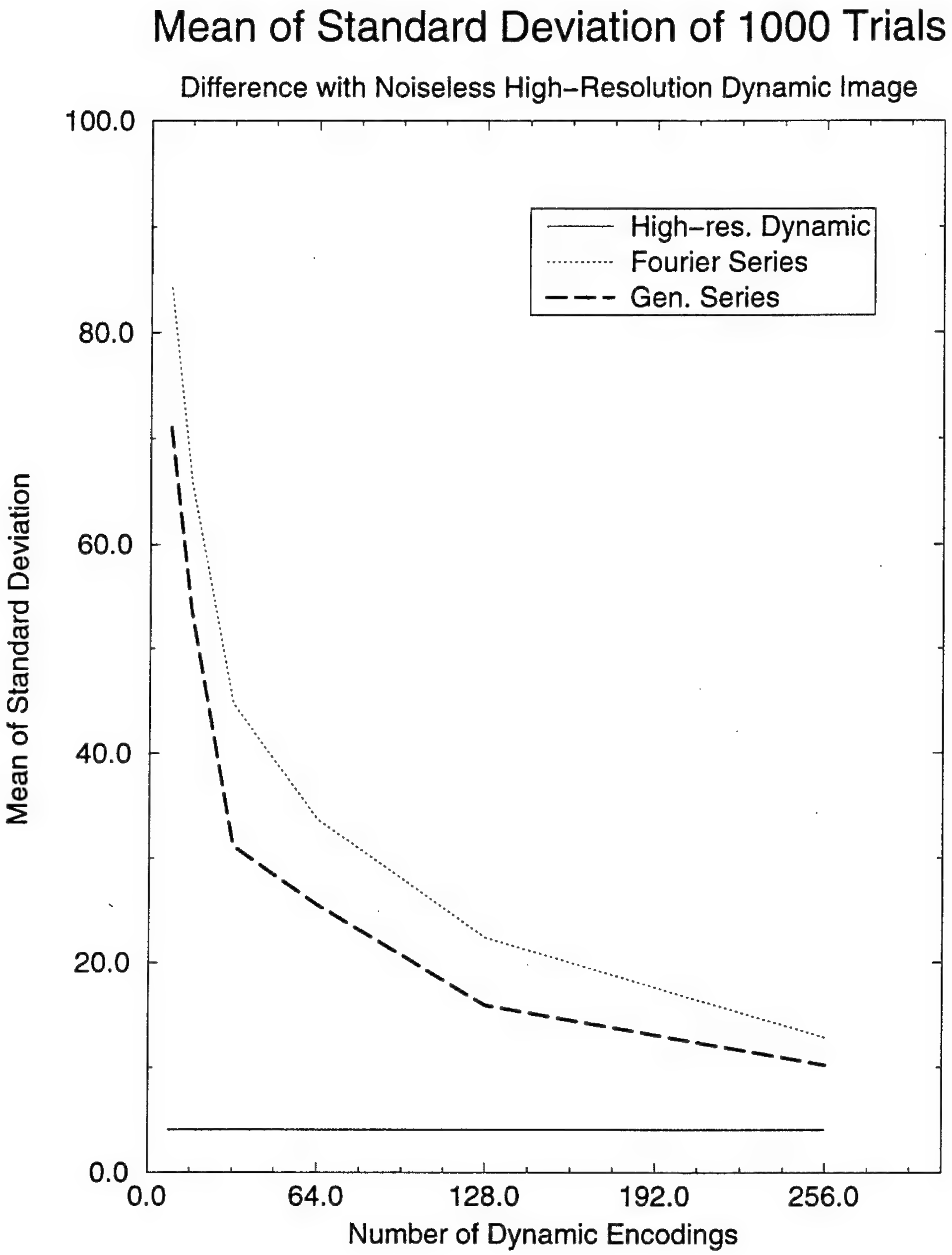

Figure A.3: SNR Behavior of Noise and Systematic Artifacts: Curves show the dependence of the mean SD of the noise and systematic artifacts, with respect to the number of dynamic encodings used in the reconstruction for the Fourier series and generalized-series. The mean SD from the high-resolution dynamic image is included as a horizontal line for comparison purposes.

high-resolution dynamic image is included as a horizontal line for comparison purposes. As would be expected, the combination of noise and systematic artifacts increases as the number of dynamic encodings decreases for both the Fourier series and the generalized series. The GS reconstructions have a smaller mean SD than the Fourier series reconstructions at all numbers of dynamic encodings due to the reduced systematic artifacts, as can be determined using both Figs. A.2 and A.3.

In summary, the noise behavior of the reduced-encoding Fourier series is better than that of the generalized-series. However, if both random noise and systematic artifacts are considered, the truncated Fourier series no longer performs better than the generalized-series. Because the quality of the resulting dynamic image is affected by both random noise and systematic artifacts, the generalized-series would be the better choice for reduced-encoding dynamic image reconstruction.

REFERENCES

[1] S. H. Heywang, A. Wolf, E. Pruss, T. Hilbertz, W. Eiermann, and W. Permanetter, "MR imaging of the breast with Gd-DTPA: Use and limitations," *Radiology*, vol. 171, pp. 95–103, 1989.

[2] W. A. Kaiser, "MR imaging examination of both breasts within 6 minutes: Technique and first results," in *Proc. RSNA 75th Ann. Meeting*, Chicago, IL, November/December 1989, p. 164.

[3] W. A. Kaiser, "MR imaging of the breast: Optimal imaging technique, results, limitations and histopathologic correlation," in *Proc. RSNA 75th Ann. Meeting*, Chicago, IL, November/December 1989, p. 230.

[4] W. A. Kaiser and O. Mittelmeier, "Breast-tissue differentiation by MRI: Results of 361 examinations in 5 years," in *Tissue Characterization in MR Imaging*, H. P. Higer and G. Bielke, Eds., New York, NY, Springer-Verlag, 1990, pp. 254–257.

[5] W. A. Kaiser, "MRM promises earlier breast cancer diagnosis," *Diagnostic Imaging*, pp. 88–93, Sept. 1992.

[6] S. E. Harms, D. P. Flamig, K. L. Hesley, and W. P. Evans, "Magnetic resonance imaging of the breast," *Magn. Reson. Q.*, vol. 8, no. 3, pp. 139–155, 1992.

[7] S. E. Harms and D. P. Flamig, "Breast: Visualizing Ca not seen by radiography," *Body MRI*, pp. 20–24, June 1993.

[8] S. E. Harms and D. P. Flamig, "MR imaging of the breast," *J. Magn. Reson. Imag.*, vol. 3, pp. 277–283, January/February 1993.

[9] J. P. Stack, O. M. Redmond, M. B. Codd, P. A. Dervan, and J. T. Ennis, "Breast disease: Tissue characterization with Gd-DTPA enhancement profiles," *Radiology*, vol. 174, pp. 491–494, 1990.

[10] W. A. Kaiser and E. Zeitler, "MR imaging of the breast: Fast imaging sequences with and without Gd-DTPA, preliminary observations," *Radiology*, vol. 170, pp. 681–686, 1989.

[11] B. A. Porter and J. P. Smith, "MRI enhances breast cancer detection and staging," *MR*, pp. 18–26,35, September/October 1993.

[12] Y. Yamashita, M. Harada, M. Torashima, M. Takahashi, K. Miyazaki, N. Tanaka, and H. Okamura, "Dynamic MR imaging of recurrent postoperative cervical cancer," *J. Magn. Reson. Imag.*, vol. 6, pp. 167–171, January/February 1996.

[13] V. Zampa, M. Mascalchi, R. Petrucci, D. Trippi, P. Petruzzi, C. Tessa, A. M. Macaluso, and C. Bartolozzi, "Gadolinium-DPTA enhancement pattern on dynamic MR imaging differentiates parotid tumors," in *Proc. Int. Soc. Magn. Reson. Med. 4th Ann. Meeting*, New York, NY, April/May 1996, p. 621.

[14] E. Furman-Haran, R. Margalit, A. F. Maretzek, and H. Degani, "Angiogenic response of MCF7 human breast cancer to hormonal treatment: Assessment by dynamic GdDTPA-enhanced MRI at high spatial resolution," *J. Magn. Reson. Imag.*, vol. 6, pp. 195–202, January/February 1996.

[15] Z.-P. Liang and P. C. Lauterbur, "Principles of magnetic resonance imaging: A signal processing perspective," ECE 380 Class Book, Dept. of Electrical and Computer Engineering, Univ. of Illinois at Urbana-Champaign, Urbana, IL, Spring 1996.

[16] G. A. Morris and R. Freeman, "Selective excitation in Fourier transform nuclear magnetic resonance," *J. Magn. Reson.*, vol. 29, pp. 433–462, 1978.

[17] P. C. Lauterbur, "Image formation by induced local interactions: Examples employing nuclear magnetic resonance," *Nature*, vol. 242, pp. 190–191, 1973.

[18] D. B. Twieg, "The k-trajectory formulation of the NMR imaging process with applications in analysis and synthesis of imaging methods," *Med. Phys.*, vol. 10, pp. 610–621, 1983.

[19] P. Mansfield, "Multi-planar image formation using NMR spin echoes," *J. Phys. C: Solid State Phys.*, vol. 10, pp. L55–L58, 1977.

[20] R. J. Ordidge, A. Howseman, R. Coxon, R. Turner, B. Chapman, P. Glover, M. Stehling, and P. Mansfield, "Snapshot imaging at 0.5T using echo-planar techniques," *Magn. Reson. Med.*, vol. 10, pp. 227–240, 1989.

[21] R. V. Mulkern, S. T. S. Wong, C. Winalski, and F. A. Jolesz, "Contrast manipulation and artifact assessment of 2D and 3D RARE sequences," *Magn. Reson. Imag.*, vol. 8, pp. 557–566, 1990.

[22] P. S. Melki, R. V. Mulkern, L. P. Panych, and F. A. Jolesz, "Comparing the FAISE method with conventional dual-echo sequences," *J. Magn. Reson. Imag.*, vol. 1, pp. 319–326, 1991.

[23] N. Higuchi, K. Oshio, Y. Imai, Y. Yuasa, K. Hiramatsu, P. S. Melki, and F. A. Jolesz, "Clinical applications of multishot RARE in abdominal MR imaging," in *Proc. Soc. Magn. Reson. Imag. 9th Ann. Meeting*, Chicago, IL, Aug. 1991, pp. 150–151.

[24] C. B. Ahn, J. H. Kim, and Z. H. Cho, "High-speed spiral-scan echo planar NMR imaging – I," *IEEE Trans. Med. Imaging*, vol. MI-5, pp. 2–7, Mar. 1986.

[25] A. Macovski and C. Meyer, "A novel fast-scanning system," in *Works-in-Progress Proc. Soc. Magn. Reson. Med. 5th Ann. Meeting*, Montreal, Quebec, Aug. 1986, p. 156.

[26] C. H. Meyer, A. Macovski, and D. G. Nishimura, "Square-spiral fast imaging," in *Proc. Soc. Magn. Reson. Med. 8th Ann. Meeting*, Amsterdam, The Netherlands, Aug. 1989, p. 362.

[27] J. I. Jackson, C. H. Meyer, D. G. Nishimura, and A. Macovski, "Selection of a convolution function for Fourier inversion using gridding," *IEEE Trans. Med. Imaging*, vol. 10, pp. 473–478, Sept. 1991.

[28] J. D. O'Sullivan, "A fast sinc function gridding algorithm for Fourier inversion in computer tomography," *IEEE Trans. Med. Imaging*, vol. MI-4, pp. 200–207, Dec. 1985.

[29] A. Takahashi, G. B. Pike, and T. M. Peters, "Applications of measured *k*-space trajectories to RF pulse design and image reconstruction," in *Proc. Soc. Magn. Reson. 2nd Ann. Meeting*, San Francisco, CA, Aug. 1994, p. 484.

[30] A. B. Kerr, J. M. Pauly, C. H. Meyer, and D. G. Nishimura, "Image quality for spiral-based sequences," in *Proc. Soc. Magn. Reson. 3rd Ann. Meeting*, Nice, France, Aug. 1995, p. 622.

[31] Z.-P. Liang and P. C. Lauterbur, "Efficient dynamic imaging using concentric scanning," in *Proc. Soc. Magn. Reson. Med. 12th Ann. Meeting*, New York, NY, Aug. 1993, p. 477.

[32] X. Zhou, Z.-P. Liang, G. P. Cofer, S. L. Gewalt, P. C. Lauterbur, and G. A. Johnson, "An FSE pulse sequence with circular sampling for MR microscopy," in *Proc. Soc. Magn. Reson. Med. 12th Ann. Meeting*, New York, NY, Aug. 1993, p. 297.

[33] J. B. Weaver and D. M. Healy, Jr., "New MRI acquisition techniques using the window Fourier transforms and the wavelet transforms," in *Proc. Soc. Magn. Reson. Med. 9th Ann. Meeting*, New York, NY, Aug. 1990, p. 414.

[34] J. B. Weaver, Y. Xu, D. Crean, and D. M. Healy, "Wavelet encoding in MR imaging," in *Proc. Soc. Magn. Reson. Med. 10th Ann. Meeting*, San Francisco, CA, Aug. 1991, p. 182.

[35] J. B. Weaver, Y. Xu, D. Crean, and D. M. Healy, "Imaging times in window Fourier transform imaging," in *Proc. Soc. Magn. Reson. Med. 10th Ann. Meeting*, San Francisco, CA, Aug. 1991, p. 857.

[36] D. M. Healy and J. B. Weaver, "Two applications of wavelet transforms in magnetic resonance imaging," *IEEE Trans. Inf. Theory*, vol. 38, pp. 840–860, 1992.

[37] X. Hu, A. H. Tewfik, and H. Garnaoui, "A new wavelet based MR imaging technique," in *Proc. Soc. Magn. Reson. Med. 11th Ann. Meeting*, Berlin, Germany, Aug. 1992, p. 432.

[38] L. P. Panych, P. D. Jakab, and F. A. Jolesz, "Progress towards real-time adaptive imaging using wavelet transform encoding," in *Proc. Soc. Magn. Reson. Med. 11th Ann. Meeting*, Berlin, Germany, Aug. 1992, p. 4513.

[39] L. P. Panych and P. D. Jakab, "Wavelet encoding in the section-select dimension," in *Proc. Soc. Magn. Reson. Imag. 10th Ann. Meeting*, New York, NY, Apr. 1992, p. 90.

[40] J. B. Weaver, Y. Xu, D. M. Healy, and J. R. Driscoll, "Wavelet-encoded MR imaging," *Magn. Reson. Med.*, vol. 24, pp. 275–287, 1992.

[41] J. B. Weaver, D. M. Healy, Jr., D. Crean, and Y. Xu, "Wavelet encoding with smooth wavelets: Short RF pulses," in *Proc. Soc. Magn. Reson. Med. 11th Ann. Meeting*, Berlin, Germany, Aug. 1992, p. 4264.

[42] J. B. Weaver, D. M. Healy, Jr., and Y. Xu, "SNR for wavelet encoded MR," in *Proc. Soc. Magn. Reson. Med. 11th Ann. Meeting*, Berlin, Germany, Aug. 1992, p. 3822.

[43] J. B. Weaver and D. M. Healy, Jr., "Adaptive wavelet encoding in cardiac imaging," in *Proc. Soc. Magn. Reson. Med. 11th Ann. Meeting*, Berlin, Germany, Aug. 1992, p. 3906.

[44] J. M. Hanson, Z.-P. Liang, and P. C. Lauterbur, "A new method for fast dynamic imaging using wavelet transforms," in *Proc. Soc. Magn. Reson. Med. 12th Ann. Meeting*, New York, NY, Aug. 1993, p. 712.

[45] K. Oshio, L. P. Panych, and F. A. Jolesz, "Wavelet encoded MR imaging (implementation)," in *Proc. Soc. Magn. Reson. Med. 12th Ann. Meeting*, New York, NY, Aug. 1993, p. 1213.

[46] L. P. Panych, P. D. Jakab, and F. A. Jolesz, "An implementation of wavelet-encoded MR imaging," in *Proc. Soc. Magn. Reson. Imag. 10th Ann. Meeting*, New York, NY, Apr. 1993, p. 26.

[47] L. P. Panych, P. D. Jakab, and F. A. Jolesz, "Implementation of wavelet-encoded MR imaging," *J. Magn. Reson. Imag.*, vol. 3, pp. 649–655, 1993.

[48] R. D. Peters and M. L. Wood, "Practical considerations for the implementation of wavelet encoding in MRI," in *Proc. Soc. Magn. Reson. Med. 12th Ann. Meeting*, New York, NY, Aug. 1993, p. 1212.

[49] L. P. Panych and F. A. Jolesz, "A dynamically adaptive imaging algorithm for wavelet-encoded MRI," *Magn. Reson. Med.*, vol. 32, pp. 738–748, 1994.

[50] L. P. Panych and F. A. Jolesz, "Theoretical comparison of resolution in wavelet and Fourier encoded MR images," in *Proc. Soc. Magn. Reson. 2nd Ann. Meeting*, San Francisco, CA, Aug. 1994, p. 776.

[51] L. P. Panych and F. A. Jolesz, "Design of optimal wavelet bases for wavelet encoded MRI," in *Proc. Soc. Magn. Reson. 2nd Ann. Meeting*, San Francisco, CA, Aug. 1994, p. 777.

[52] N. Gelman, M. L. Wood, and R. D. Peters, "Three dimensional gradient echo imaging using wavelet encoding," in *Proc. Soc. Magn. Reson. 3rd Ann. Meeting*, Nice, France, Aug. 1995, p. 662.

[53] R. D. Peters and M. L. Wood, "Multilevel wavelet-encoded MR imaging," in *Proc. Soc. Magn. Reson. 3rd Ann. Meeting*, Nice, France, Aug. 1995, p. 194.

[54] N. Gelman and M. L. Wood, "Wavelet encoding for improved SNR and retrospective slice thickness adjustment," in *Proc. Int. Soc. Magn. Reson. Med. 4th Ann. Meeting*, New York, NY, April/May 1996, p. 1535.

[55] W.-L. Hwang, N.-K. Chen, C. Chen, and H. N. Yeung, "Application of wavelet decomposition in dynamic MRI," in *Proc. Int. Soc. Magn. Reson. Med. 4th Ann. Meeting*, New York, NY, April/May 1996, p. 1650.

[56] L. P. Panych, "Theoretical comparison of Fourier and wavelet encoding in magnetic resonance imaging," *IEEE Trans. Med. Imaging*, vol. 15, pp. 141–153, Apr. 1996.

[57] R. D. Peters and M. L. Wood, "Multilevel wavelet-transform encoding in MRI," *J. Magn. Reson. Imag.*, vol. 6, pp. 529–540, 1996.

[58] Y. Cao and D. N. Levin, "On the relationship between feature-recognizing MRI and MRI encoded by singular value decomposition," *Magn. Reson. Med.*, vol. 33, pp. 140–142, Jan. 1995.

[59] Y. Cao, D. N. Levin, and L. Yao, "Locally focused MRI," *Magn. Reson. Med.*, vol. 34, pp. 858–867, Dec. 1995.

[60] L. P. Panych, C. Oesterle, G. P. Zientara, and J. Hennig, "Implementation of a fast gradient-echo SVD encoding technique for dynamic imaging," in *Proc. Soc. Magn. Reson. 3rd Ann. Meeting*, Nice, France, Aug. 1995, p. 663.

[61] L. P. Panych, C. Oesterle, G. P. Zientara, and J. Hennig, "Implementation of a fast gradient-echo SVD encoding technique for dynamic imaging," *Magn. Reson. Med.*, vol. 35, pp. 554–562, 1995.

[62] L. P. Panych, W. E. Kyriakos, G. P. Zientara, and F. A. Jolesz, "Dynamically adaptive MRI methods for following change occuring within a reduced field-of-view," in *Proc. Soc. Magn. Reson. 3rd Ann. Meeting*, Nice, France, Aug. 1995, p. 193.

[63] L. P. Panych, P. Saiviroonporn, R. V. Mulkern, G. P. Zientara, and F. A. Jolesz, "Non-Fourier encoding with multiple spin echoes," in *Proc. Int. Soc. Magn. Reson. Med. 4th Ann. Meeting*, New York, NY, April/May 1996, p. 115.

[64] L. P. Panych, P. Saiviroonporn, G. P. Zientara, and F. A. Jolesz, "Implementation of a 3D interleaved echo-planar method for SVD encoded MRI," in *Proc. Int. Soc. Magn. Reson. Med. 4th Ann. Meeting*, New York, NY, April/May 1996, p. 387.

[65] P. Saiviroonporn, G. P. Zientara, L. P. Panych, and F. A. Jolesz, "Real-time computations for dynamically adaptive SVD encoded MRI," in *Proc. Soc. Magn. Reson. 3rd Ann. Meeting*, Nice, France, Aug. 1995, p. 665.

[66] G. P. Zientara, L. P. Panych, and F. A. Jolesz, "Dynamically adaptive MRI with encoding by singular value decomposition," *Magn. Reson. Med.*, vol. 32, pp. 268–274, 1994.

[67] G. P. Zientara, L. P. Panych, and F. A. Jolesz, "Keyhole SVD encoded MRI," in *Proc. Soc. Magn. Reson. 2nd Ann. Meeting*, San Francisco, CA, Aug. 1994, p. 778.

[68] G. P. Zientara, L. P. Panych, and F. A. Jolesz, "Multi-resolution SVD encoding for dynamically adaptive MRI," in *Proc. Soc. Magn. Reson. 2nd Ann. Meeting*, San Francisco, CA, Aug. 1994, p. 800.

[69] G. P. Zientara, L. P. Panych, and F. A. Jolesz, "Lanczos spatial encodings for dynamically adaptive MRI," in *Proc. Soc. Magn. Reson. 3rd Ann. Meeting*, Nice, France, Aug. 1995, p. 664.

[70] G. P. Zientara, L. P. Panych, P. Saiviroonporn, and F. A. Jolesz, "MR fluoroscopy using near-optimal adaptive spatial encoding," in *Proc. Int. Soc. Magn. Reson. Med. 4th Ann. Meeting*, New York, NY, April/May 1996, p. 1495.

[71] Z.-P. Liang, F. E. Boada, R. T. Constable, E. M. Haacke, P. C. Lauterbur, and M. R. Smith, "Constrained reconstruction methods in MR imaging," *Reviews Magn. Reson. Med.*, vol. 4, pp. 67–185, 1992.

[72] Z.-P. Liang and P. C. Lauterbur, "Improved temporal/spatial resolution in functional imaging through generalized series reconstruction," in *Works-in-Progress Proc. Soc. Magn. Reson. Imag. 10th Ann. Meeting*, New York, NY, Aug. 1992, p. S15.

[73] Z.-P. Liang and P. C. Lauterbur, "An efficient method for dynamic magnetic resonance imaging," *IEEE Trans. Med. Imaging*, vol. 13, pp. 677–686, Dec. 1994.

[74] J. J. van Vaals, H. H. Tuithof, and W. T. Dixon, "Increased time resolution in dynamic imaging," in *Proc. Soc. Magn. Reson. Imag. 10th Ann. Meeting*, New York, NY, Aug. 1992, p. 44.

[75] J. E. Bishop, I. Soutar, W. Kucharczyk, and D. B. Plewes, "Rapid sequential imaging with shared-echo fast spin-echo MR imaging," in *Works-in-Progress Proc. Soc. Magn. Reson. Imag. 10th Ann. Meeting*, New York, NY, Aug. 1992, p. S22.

[76] S. G. Mallat, "A theory for multiresolution signal decomposition: The wavelet representation," *IEEE Trans. Patt. Anal. Mach. Intell.*, vol. 11, pp. 674–693, July 1989.

[77] I. Daubechies, "Orthonormal bases of compactly supported wavelets," *Comm. Pure Appl. Math.*, vol. XLI, pp. 909–996, 1988.

[78] K. S. Arun, "Fundamentals of digital signal and spectral analysis," ECE 413 Class Book, Dept. of Electrical and Computer Engineering, Univ. of Illinois at Urbana-Champaign, Urbana, IL, Spring 1992.

[79] M. Antonini, M. Barlaud, P. Mathieu, and I. Daubechies, "Image coding using wavelet transform," *IEEE Trans. Image Proc.*, vol. 1, pp. 205–220, Apr. 1992.

[80] J. D. Villasenor, B. Belzer, and J. Liao, "Wavelet filter evaluation for image compression," *IEEE Trans. Image Proc.*, vol. 2, pp. 1053–1060, Aug. 1995.

[81] D. B. Plewes, J. Bishop, I. Soutar, and E. Cohen, "Errors in quantitative dynamic three-dimensional Keyhole MR imaging of the breast," *J. Magn. Reson. Imag.*, vol. 5, pp. 361–364, 1995.

[82] D. E. Egerter, "Keyhole imaging enhances dynamic contrast studies," *MR*, pp. 8,13,49, Winter 1992.

[83] X. Hu, "On the "keyhole" technique," *J. Magn. Reson. Imag.*, vol. 4, p. 231, Mar. 1994.

[84] T. A. Spraggins, "Simulation of spatial and contrast distortions in keyhole imaging," *Magn. Reson. Med.*, vol. 31, pp. 320–322, 1994.

[85] Z.-P. Liang and P. C. Lauterbur, "Efficient time-sequential imaging through generalized series modeling: A simulation analysis," in *Works-in-Progress Proc. Soc. Magn. Reson. Med. 11th Ann. Meeting*, Berlin, Germany, Aug. 1992, p. 4266.

[86] J. M. Hanson, Z.-P. Liang, R. L. Magin, J. L. Duerk, and P. C. Lauterbur, "A comparison of RIGR and SVD dynamic MRI methods," *Magn. Reson. Med.*, in press, 1997.

[87] J. M. Hanson, Z.-P. Liang, E. Wiener, and P. C. Lauterbur, "Fast dynamic imaging using two reference images," in *Proc. Soc. Magn. Reson. 3rd Ann. Meeting*, Nice, France, Aug. 1995, p. 97.

[88] J. M. Hanson, Z.-P. Liang, E. Wiener, and P. C. Lauterbur, "Fast dynamic imaging using two reference images," *Magn. Reson. Med.*, vol. 36, pp. 172–175, July 1996.

[89] N. Ahuja, "A transform for detection of multiscale image structure," in *Proc. DARPA Image Understanding Workshop*, Washington, DC, Apr. 1993, pp. 893–902.

[90] N. Ahuja, "A transform for detection of multiscale image structure," in *Proc. Comp. Vision Patt. Recog.*, New York, NY, June 1993, pp. 780–781.

[91] R. L. Ehman and J. P. Felmlee, "Adaptive technique for high-definition MR imaging of moving structures," *Radiology*, vol. 173, no. 1, pp. 258–263, 1989.

[92] Y. Wang, R. C. Grimm, S. J. Riederer, and R. L. Ehman, "Algorithms to extract motion information from navigator echoes," in *Proc. Soc. Magn. Reson. 3rd Ann. Meeting*, Nice, France, Aug. 1995, p. 751.

[93] Z. W. Fu, Y. Wang, R. C. Grimm, P. J. Rossman, J. P. Felmlee, S. J. Riederer, and R. L. Ehman, "Orbital navigator echoes for motion measurements in magnetic resonance imaging," *Magn. Reson. Med.*, vol. 34, pp. 746–753, 1995.

[94] Y. Wang, R. C. Grimm, J. P. Felmlee, S. J. Riederer, and R. L. Ehman, "Algorithms for extracting motion information from navigator echoes," *Magn. Reson. Med.*, vol. 36, pp. 117–123, 1996.

[95] C. C. Lee, C. R. Jack, Jr., R. C. Grimm, P. J. Rossman, J. P. Felmlee, R. L. Ehman, and S. J. Riederer, "Real-time adaptive motion correction in functional MRI," *Magn. Reson. Med.*, vol. 36, pp. 436–444, 1996.

CURRICULUM VITAE

Jill M. Hanson

Work Address
Biomedical Magnetic Resonance Laboratory
1307 West Park Street
Urbana, IL 61801
(217) 244–0600 / (217) 244–1330 FAX

Home Address
1407 East Pennsylvania Avenue
Urbana, IL 61801-5322
(217) 337–1239
jill@bmrl.med.uiuc.edu

Education

PH.D., ELECTRICAL ENGINEERING, 1997
Dissertation: "Reduced-Encoding Dynamic Imaging"
University of Illinois at Urbana-Champaign — Urbana, IL

M.S., ELECTRICAL ENGINEERING, 1991
Stanford University — Stanford, CA

B.E.E., ELECTRICAL ENGINEERING, 1989
University of Dayton — Dayton, OH

Academic Experience

BIOMEDICAL MAGNETIC RESONANCE LABORATORY — Urbana, IL
1992–present
Graduate Research Assistant

UNIVERSITY OF ILLINOIS AT URBANA-CHAMPAIGN — Urbana, IL
1993 fall, 1996 spring
Teaching Assistant, Department of Electrical and Computer Engineering

STANFORD UNIVERSITY — Stanford, CA
1989 fall–1990 spring
Teaching Assistant, Department of Electrical Engineering

Industrial Experience

WRIGHT PATTERSON AIR FORCE BASE — Fairborn, OH
1991 summer
Fellowship Summer Research Student

DELCO PRODUCTS, GENERAL MOTORS — Dayton, OH
1989, 1990 summers
New Product Development Engineer

INLAND DIVISION, GENERAL MOTORS — Dayton, Vandalia, OH; Matamoros, Mexico
1984–1989
Cooperative education student in various departments including new product development, product design in several product lines, production engineering, purchasing and personnel.

HOBART CORPORATION — Dayton, OH
1983 summer
Engineering and Science Careers Program high school student

Awards

Army Breast Cancer Research Program Predoctoral Fellowship, 1994-1997

Incomplete List of Teachers Rated as Excellent by Their Students, 1996

ISMRM Student Travel Stipend Award, 1996

SMRM Student Travel Stipend Award, 1993

U.S. Air Force Laboratory Graduate Fellowship, 1990-1993

Graduated Summa Cum Laude, 1989

Thomas Armstrong Award for "Outstanding Electrical Engineering Achievement", 1989

Tau Beta Pi, 1986

Eta Kappa Nu, 1986

"Dayton Area" Full Tuition Scholarship, 1984-1989

Ohio Board of Regents Scholarship, 1984-1989

Ohio Choice Grant, 1984-1989

Publications

J. M. Hanson, Z.-P. Liang, R. L. Magin, J. L. Duerk, and P. C. Lauterbur, "A comparison of RIGR and SVD dynamic imaging methods," *Magn. Reson. Med.*, in press, 1997.

C. P. Hess, H. Jiang, J. M. Hanson, and Z.-P. Liang, "A software system for interactive MR signal processing," *Magn. Reson. Imaging* 15(1), 127-130, 1997.

J. M. Hanson, Z.-P. Liang, and P. C. Lauterbur, "Fast dynamic imaging using two reference images," *Magn. Reson. Med.* 36, 172-175, 1996.

J. M. Hanson, Z.-P. Liang, R. L. Magin, J. L. Duerk, and P. C. Lauterbur, "A comparison of RIGR and SVD dynamic MRI methods," in *Proc. ISMRM, 4th Annual Meeting,* New York, NY, 1996, p. 118.

J. M. Hanson, Z.-P. Liang, and P. C. Lauterbur, "Improved RIGR dynamic imaging using explicit boundary constraints with application to breast imaging," in *Proc. SMR, 3rd Annual Meeting,* Nice, France, 1995, p. 1596.

J. M. Hanson, Z.-P. Liang, E. Wiener, and P. C. Lauterbur, "Fast dynamic imaging using two reference images," in *Proc. SMR, 3rd Annual Meeting,* Nice, France, 1995, p. 97.

H. Jiang, C. P. Hess, J. M. Hanson, C. S. Potter, and Z.-P. Liang, "V: A software system for MRI signal processing," in *Proc. SMR, 3rd Annual Meeting,* Nice, France, 1995, p. 701.

Z.-P. Liang, J. M. Hanson, C. S. Potter, and Paul C. Lauterbur, "Efficient high-resolution dynamic imaging with explicit boundary constraints," in *Proc. SMR, 2nd Annual Meeting,* San Francisco, CA, 1994, p. 53.

J. M. Hanson, Z.-P. Liang, and P. C. Lauterbur, "A new method for fast dynamic imaging using wavelet transforms," in *Proc. SMRM, 12th Annual Meeting,* New York, NY, 1993, p. 712.